Evolution of Idealized Vortices in Monsoon-Like Shears: Application to Monsoon Depressions✐

MICHAEL DIAZ[a] AND WILLIAM R. BOOS[a,b]

[a] *Department of Earth and Planetary Science, University of California, Berkeley, Berkeley, California*
[b] *Climate and Ecosystem Sciences Division, Lawrence Berkeley National Laboratory, Berkeley, California*

ABSTRACT: This study examines processes fundamental to the development of South Asian monsoon depressions using an array of integrations of an idealized convection-permitting numerical model. In each integration, a wave of initially small amplitude is subjected to a different amount of vertical and meridional wind shear, with temperature and moisture fields constructed according to realistic constraints. Based on the evolution of this disturbance into monsoon depression–like vortices, two features of the background environment emerge as important: the low-level gradient of moist static energy (MSE) and the low-level meridional shear. As the low-level MSE gradient steepens, the disturbance becomes stronger and produces more rain. This strengthening results from the interaction of the vortex with latent heat release by convection that is in turn organized by positive MSE advection in the northerly flow west of the vortex. In this region of advection, moister air from the north ascends along upward-sloping isentropes, driving moist convection. The disturbance also becomes stronger with increasing meridional shear, which makes the environment more barotropically unstable. The absence of either of these two features of the background environment prevents substantial growth of the disturbance. Our results suggest that monsoon depression growth in South Asia is fostered by the coexistence of a strong low-level MSE gradient with strong meridional wind shear associated with the monsoon trough.

KEYWORDS: Asia; Baroclinic flows; Convection; Cyclogenesis/cyclolysis; Monsoons; Mesoscale models

1. Introduction

Low pressure systems in multiple regions of the tropics have been labeled as monsoon depressions. Perhaps the most famous of these are those that develop over the Bay of Bengal during the Indian monsoon, where they have been catalogued for well over a century (Mooley and Shukla 1989). What makes this region so uniquely conducive to monsoon depression formation remains an area of active research (Ditchek et al. 2016). Many studies have highlighted some feature of the background environment as being of key importance [see Diaz and Boos (2019a) for a detailed overview]. For example, in contrast with most of the tropics, this region's climatology is dominated by strong easterly vertical wind shear, with an accompanying temperature gradient in approximate thermal wind balance. Although this baroclinicity usually prevents tropical cyclogenesis, past studies have cited reasons why it could favor monsoon depressions, including through baroclinic instability (Saha and Chang 1983; Moorthi and Arakawa 1985), its link to quasigeostrophic ascent (Rao and Rajamani 1970), or its role in forcing isentropic ascent (Adames and Ming 2018b). Other studies have argued that the locally enhanced vorticity of the monsoon trough can become barotropically unstable, allowing disturbances to gain energy from the background meridional shear (Nitta and Masuda 1981). More recently, the northward-directed gradient of moisture that characterizes this region has

been hypothesized to favor monsoon depression development through a moisture–vortex instability (Adames and Ming 2018a). Finally, since they most commonly form over ocean, other studies have argued that surface heat and moisture fluxes are important for their intensification (Fujinami et al. 2020).

Building upon these studies, our recent work has argued that monsoon depressions can form through a variant of moist barotropic instability that requires vertical shear (Diaz and Boos 2019b). In this paradigm, vortices draw energy from both the meridional shear of the monsoon trough and through coupling with moist convection. This convection is maintained by ascent forced by the vortex interacting with the vertically sheared environment. Following previous studies, this ascent is explained using the quasigeostrophic (QG) omega equation. Latent heating from convection brings an otherwise weakly stable background flow to a state of barotropic instability. This mechanism does not involve baroclinic instability and does not require interactive surface heat fluxes. A different growth mechanism for monsoon depressions was presented by Adames and Ming (2018b). Using idealized experiments, they reproduced monsoon depression–like disturbances and argued that their convection was organized by their interaction with the time-mean moist static energy (MSE) gradient. From an MSE budget, they concluded that the presence of a temperature gradient led to isentropic ascent west of the circulation center. This ascent advected moisture vertically, leading to an environment favorable for convection, whose associated vortex stretching promoted growth of the larger-scale vortex. Whereas Adames and Ming (2018b) found that vertical advection dominated the moisture tendency, the moisture–vortex instability in the analytic model of Adames and Ming (2018a) relied on horizontal moisture advection. Neither Adames

---

✐ Supplemental information related to this paper is available at the Journals Online website: https://doi.org/10.1175/JAS-D-20-0286.s1.

Corresponding author: Michael Diaz, mldiaz@ncsu.edu

and Ming (2018b) nor Adames and Ming (2018a) argued for any role by barotropic instability.

In summary, despite recent progress in our understanding of monsoon depressions, unanswered questions remain. For example, what is the importance of barotropic instability compared with convection in realizing vortex growth? Which of the above mechanisms best describes how the vortex couples with convection? A key drawback of studies such as Diaz and Boos (2019b) and Adames and Ming (2018a) is that the complicated background flows they use make it difficult to unambiguously isolate particular physical processes. At the other extreme, while simple analytical models such as that presented by Adames and Ming (2018b) excel at highlighting mechanisms, they could be oversimplifications of reality. Thus, it would be instructive to have a background environment that can be systematically altered to vary wind shears and MSE gradients in order to test how growing disturbances respond. The goal of this study is to investigate the role that such environmental factors play in the development of monsoon depressions using a set of idealized model experiments, and then deduce which of the aforementioned processes most plausibly explain their growth.

2. Methods

This study uses the numerical model developed by Diaz and Boos (2019a) and expanded upon by Diaz and Boos (2019b). The advantage of this model is that it separates the atmosphere into a basic state and perturbations, allowing us to perform experiments wherein we prescribe a background environment (the basic state) and examine how a monsoon depression–like vortex (the perturbation) evolves within it.

a. Model equations

Equations for momentum, temperature, pressure, and water mixing ratios used in the numerical model are

$$\frac{\partial \mathbf{u}'}{\partial t} = -(\overline{\mathbf{U}} + \mathbf{u}') \cdot \nabla \mathbf{u}' - \mathbf{u}' \cdot \nabla \overline{\mathbf{U}} - \nabla \phi' + b' \hat{\mathbf{k}} - f \hat{\mathbf{k}} \times \mathbf{v}' + \mathbf{T}'_{\mathbf{u}},$$
(1a)

$$\frac{\partial \theta'}{\partial t} = -(\overline{\mathbf{U}} + \mathbf{u}') \cdot \nabla \theta' - \mathbf{u}' \cdot \nabla \overline{\theta} - w' \frac{d\theta_0}{dz} + M'_\theta + T'_\theta,$$
(1b)

$$\frac{\partial^2 \phi'}{\partial x^2} + \frac{\partial^2 \phi'}{\partial y^2} + \frac{\partial}{\partial z}\left(\rho_0 \frac{\partial \phi'}{\partial z}\right) = \nabla \cdot (\rho_0 G\{\mathbf{u}'\}),$$
(1c)

$$\frac{\partial q'_v}{\partial t} = -(\overline{\mathbf{U}} + \mathbf{u}') \cdot \nabla q'_v - \mathbf{u}' \cdot \nabla \overline{q}_v - w' \frac{dq_0}{dz} + M'_{q_v} + T'_{q_v},$$
(1d)

$$\frac{\partial q_c}{\partial t} = -(\overline{\mathbf{U}} + \mathbf{u}') \cdot \nabla q_c + M_c + T_c,$$
(1e)

$$\frac{\partial q_{r,s,i}}{\partial t} = -(\overline{\mathbf{U}} + \mathbf{u}') \cdot \nabla q_{r,s,i} - w_t \frac{\partial q_{r,s,i}}{\partial z} + M_{q_{r,s,i}} + T_{q_{r,s,i}},$$
(1f)

where $\mathbf{u} = \langle u, v, w \rangle$ represents the three-dimensional velocity field, $\mathbf{v} = \langle u, v \rangle$ the two-dimensional velocity field, θ the potential temperature, ρ the density, $\phi = p/\rho_0$ the pressure normalized by density, q_v the water vapor mixing ratio, q_c the cloud water mixing ratio, $q_{r,s,i}$ the rain, snow, or ice water

mixing ratio, and w_t the terminal velocity of rain, snow, or ice. Primes denote perturbation values, bars denote basic-state values, and the zero subscripts denote base-state values. The *base* state varies in only the vertical direction and is a resting state used to make the standard anelastic approximation, whereas the *basic* state can vary in all three dimensions and is used to impose a nonresting environment in which perturbations grow. Microphysical processes, e.g., condensation and evaporation, are represented by M, and tendencies from surface fluxes and subgrid-scale turbulence by T. The buoyancy term (b') is defined in terms of virtual potential temperature,

$$b' = g\left(\frac{\theta'}{\theta_0} + 0.61 q'_v - q_c - q_r - q_i - q_s\right).$$
(2)

Unlike Diaz and Boos (2019b), which uses a warm rain microphysical parameterization based on Kessler (1969), this study uses an ice microphysical parameterization based on Rutledge and Hobbs (1983), with the improvements suggested by Hong et al. (2004). The subgrid-scale turbulence parameterization is described in Diaz and Boos (2019b). To isolate the physical processes associated with wind shear and gradients of temperature and moisture, we exclude interactive surface fluxes of heat and moisture. However, as discussed in Diaz and Boos (2019b), there are implicit surface fluxes necessary to maintain the basic state. We will explore the impact of interactive surface fluxes in a forthcoming study.

b. Experimental design

1) BASIC STATES

Each basic state consists of two zonally uniform components. The first is a profile of zonal wind that varies only in height. The second is a monsoon trough–like feature, with a region of enhanced meridional shear whose maximum amplitude is concentrated near the surface. These two components are added together to create a basic-state wind field with a mixture of vertical and meridional shear that is zonally symmetric in the east–west direction with zero meridional wind. The temperature and moisture fields are then derived based on realistic constraints.

The first component of the basic state is defined in terms of its vertical shear as

$$\frac{\partial \overline{U}}{\partial z}(z) = \begin{cases} S_L + z \dfrac{S_U - S_L}{h_U - h_L} & z \le h_U \\ S_U & z > h_U \end{cases},$$
(3a)

$$S_L \equiv \partial_z \overline{U}(h_L),$$
(3b)

$$S_U \equiv \partial_z \overline{U}(h_U),$$
(3c)

$$\overline{U}(h_0) = 3\,\mathrm{m\,s}^{-1},$$
(3d)

where $h_L = 0\,\mathrm{km}$, $h_U = 16.6\,\mathrm{km}$, and $h_0 = 4.0\,\mathrm{km}$. This functional form is linear and allows us to concentrate the vertical shear in either the lower (S_L) or upper (S_U) troposphere, resulting in vertical profiles of $\overline{U}$ that are parabolic. The second component of the basic state, the monsoon trough–like feature,

is a surface-intensified strip of vorticity, whose relative vorticity is defined as

$$\zeta(y,z) = \zeta_0 \left[\cos\left(-\pi + 2\pi \frac{y - y_0}{y_1 - y_0} \right) + 1 \right]$$
$$\times \left[\cos\left(-0.1\pi + 1.2\pi \frac{z - z_0}{z_1 - z_0} \right) + 1 \right], \qquad (4)$$

defined on the interval y_0 to y_1 where $y_0 = 18°N$, $y_1 = 21°N$, $z_0 = 0\,m$, and $z_1 = 17.0\,km$. The wind field is then obtained by solving

$$\frac{\partial^2 \overline{U}}{\partial y^2} = \zeta(y, z) \qquad (5)$$

with periodic lateral boundaries in the zonal direction and zero-gradient boundaries in the north and south. The final basic-state zonal wind field is constructed by adding $\overline{U}$ from Eq. (3) and $\overline{U}$ from Eq. (5). This procedure leaves us with three tunable parameters for the basic state, namely, S_L, S_U, and ζ_0, which control the strength of the lower-level vertical shear, the upper-level vertical shear, and the lower-level meridional shear, respectively. For succinctness, these will all be expressed as dimensionless quantities throughout this manuscript, by normalizing S_L and S_U by $1\,m\,s^{-1}\,km^{-1}$, and by normalizing ζ_0 by $1 \times 10^{-4}\,s^{-1}$. As will be discussed shortly, S_L and S_U can also be thought of as controls on the lower- and upper-level temperature and moisture gradient. However, it should be noted that since S_L and S_U affect the shear over the entire interval between h_L and h_U, S_U has some effect on the lower-level shear and S_L has some effect on the upper-level shear. For example, incrementing S_L by 1.0 alters the shear at 2.0 km by $0.43\,m\,s^{-1}\,km^{-1}$, while incrementing S_U by 1.0 alters the shear at 2.0 km by $0.12\,m\,s^{-1}\,km^{-1}$. Additionally, since Eq. (4) alters the meridional shear more strongly at lower levels, it also adds vertical shear to the basic state. However, it does so in a manner different from S_U and S_L. For the range of parameters we will use, it increases vertical shear south of the monsoon trough axis at 20°N while decreasing it to the north. At 20°N, Eq. (4) does not impact vertical shear.

For a given wind field, we use thermal wind balance to construct the basic-state temperature and pressure fields. Since the thermal wind equation is expressed in terms of gradients, we must specify the vertical temperature profile at one point. The structure of this profile is important because, along with humidity, it determines the stability of the atmosphere to moist convection. To define a representative profile, we use the values of temperature and mixing ratio at 20°N, 88°E from the basic state of Diaz and Boos (2019b), which was constructed to represent the pregenesis environment of monsoon depressions (Fig. 1). This point is near the track density maximum of observed monsoon depressions and its latitude corresponds to where the vortices in our simulations are centered. The profile in Fig. 1 is used to define θ_0 and q_0 in Eqs. (1b) and (1d), with $\overline{\theta}$ and $\overline{q_v}$ being set to zero at 20°N. Hence, the vertical profiles of total temperature and humidity among all of our experiments are identical at 20°N. The surface pressure at this latitude is set to 1002.0 hPa.
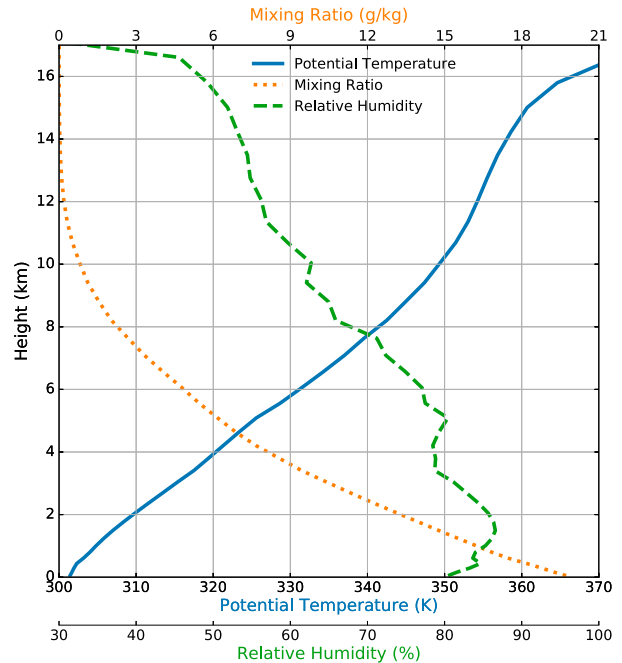
FIG. 1. Base-state profile of potential temperature (θ_0), mixing ratio (q_0), and relative humidity.

Creating the meridional moisture gradient is somewhat trickier. It requires a compromise between a method that can readily be applied to a wide range of basic states and one that accurately approximates the conditions in the South Asian monsoon. Unlike some theoretical models in which the moisture and temperature gradients are decoupled (e.g., Monteiro and Sukhatme 2016; Adames and Ming 2018a), the extent to which the moisture gradient in our simulation can be increased in the absence of a temperature gradient is limited by the Clausius–Clapeyron equation and the constraint that the relative humidity remains below 100%. Thus, to create the humidity field outside of the base latitude of 20°N, we assume constant relative humidity between 15° and 26°N and adjust the mixing ratio accordingly. Given that temperature increases going northward, this adjustment yields a northward-directed moisture gradient. To the north and south of this region, the relative humidity is decreased linearly by 10% from 26° to 30°N and from 15° to 5°N. This decrease ensures that the environment does not become overly unstable to moist convection in the northern and southern regions of the domain, which lie outside our primary region of interest. We found using relative humidity to control the moisture field superior to using mixing ratio, because modifying the latter directly is more prone to creating unrealistic humidity profiles.

One complication resulting from the effect of ζ_0 on the vertical shear (and thus on the temperature gradient) is that increasing ζ_0 will also increase the moisture gradient if the procedure described above is followed. This dependence is undesirable since our results prove to be quite sensitive to both the moisture distribution and the meridional shear. To help alleviate this problem, we use the component of the temperature field in thermal wind balance with the vertical shear for
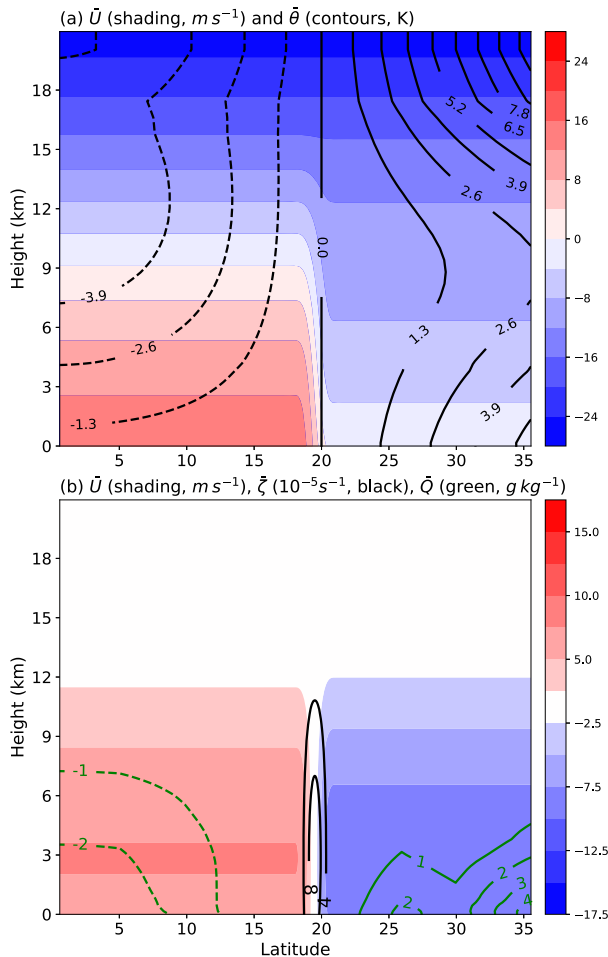
FIG. 2. Cross sections of basic state. (a) Basic-state zonal wind (shading, $\overline{U}$, m s^{-1}) and potential temperature (contours, $\overline{\theta}$, K) for $\zeta_0 = 1.0$, $S_L = -1.0$, and $S_U = -2.0$ and (b) basic-state zonal wind (shading, $\overline{U}$, m s^{-1}), vorticity (black contours, $\overline{\zeta}$, 10^{-5} s^{-1}), and mixing ratio (green contours, $\overline{q_v}$, g kg^{-1}) for $\zeta_0 = 1.0$, $S_L = 0.0$, and $S_U = 0.0$. Dashed contours show negative values. The basic-state potential temperature and mixing ratio shown here are horizontal deviations from the base state shown in Fig. 1.

$\zeta_0 = 1.0$ to set the moisture field for all of our experiments. As a result, changes to ζ_0 affect the relative humidity field instead of the mixing ratio field. Thus, changing ζ_0 does not affect the moisture gradient and has a minimal effect on the MSE gradient.

Two sample basic states are shown in Fig. 2. Figure 2a shows $\overline{U}$ and $\overline{\theta}$ for $S_L = 1.0$, $S_U = -2.0$, and $\zeta_0 = 1.0$. These settings yield a northward temperature gradient and easterly vertical shear. Westerly flow dominates near the surface and easterly flow dominates aloft, with a well-defined monsoon trough axis near 20°N. These are all classic features of a monsoon climate. Figure 2b shows $\overline{U}$, $\overline{\zeta}$, and $\overline{Q}$ for a state that isolates the low-level monsoon trough with $S_L = 0.0$, $S_U = 0.0$, and $\zeta_0 = 1.0$. As previously discussed, in addition to providing meridional shear, nonzero values of ζ_0 also produce some vertical shear. With this shear changing its direction at the monsoon trough axis, a

sharp meridional gradient of vertical shear results when added to the contribution of shear from S_L and S_U (cf. Fig. 2a). This gradient is a realistic feature of the observed South Asian monsoon. Also note the northward moisture gradient in Fig. 2b. As pointed out in section 1, some have argued that this feature is important for monsoon depression growth. For reference, all of the basic states used in this study are available in the online supplementary material (Figs. S1–S4).

2) INITIAL PERTURBATION

We initialize each simulation with the fastest growing dry linear normal mode of wavenumber 2 for a horizontal shear of $\zeta_0 = 1.0$ and vertical shears of zero (the basic state shown in Fig. 2b). Excluding the vertical shear in the normal mode calculation ensures that each experiment starts with the same initial condition, and having two wavelengths is beneficial because it provides us with an ensemble of two growing disturbances. This mode is barotropically unstable and will be scaled to give v' a maximum value of 5 m s^{-1}. The initial moisture field q'_v will be set to zero. An alternative way to initialize our experiments would be to use a vortex. We chose to use a normal mode instead, because it requires fewer arbitrary parameters to set, such as size, location, and structure. We also found that a vortex tends to rapidly disperse along the basic-state vorticity gradients, leading to multiple disturbances in various stages of growth. This evolution is more difficult to analyze, especially when comparing different experiments.

3) MODEL CONFIGURATION

Each simulation is run for 6 days and uses a grid spacing of 5 km × 5 km with 1035 grid points in the east–west direction, 777 in the north–south direction, and 43 in the vertical. The vertical coordinate uses a stretched grid. Although the grid spacing used is perhaps larger than ideal for a convection-permitting simulation, the fact that the convection is organized by synoptic-scale processes justifies this somewhat coarser resolution.

To help isolate the impact of moist convection, we conduct two sets of experiments for each basic state: one with moisture as previously described and one with zero moisture, effectively eliminating microphysical processes. For convenience, we will refer to these as "dry" and "moist" experiments.

3. Results

a. Sample case

We start by illustrating a sample case from a region of parameter space that favors robust, monsoon depression–like vortices. Figure 3 shows the simulation for $\zeta_0 = 1.5$, $S_L = -1.0$, and $S_U = -2.0$ at hour 78. The background map is drawn for reference only; i.e., the coastal outlines do not indicate changes in surface characteristics. This vortex has a minimum sea level pressure of 996.2 hPa and exhibits many features of observed monsoon depressions. The strongest convection lies to the southwest of the circulation center, where the northerly flow of the low pressure system interacts with the northern edge of the low-level westerlies (Fig. 3b). Additionally, it has a warm core
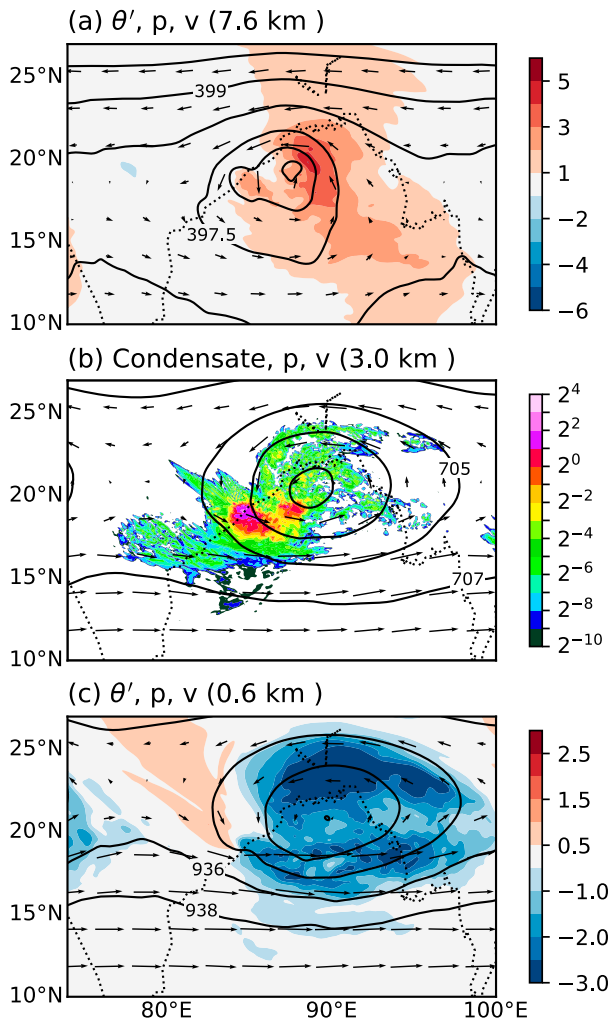
FIG. 3. Sample monsoon depression from $\zeta_0 = 1.5$, $S_L = -1.0$, and $S_U = -2.0$ at hour 78. (a) Perturbation potential temperature (shading, θ', K), total pressure (contoured by 0.75 hPa), and wind vectors at 7.6 km. (b) The vertically integrated condensate from the surface to 15 km (shading, $q_c + q_i + q_s + q_r$, g kg^{-1}), total pressure (contoured by 2.0 hPa), and wind vectors at 3.0 km, (c) As in (a), but at 0.6 km with pressure contoured by 2.0 hPa. The background map is for scale reference only and has no effect on the simulations.

aloft (Fig. 3a) and a cold core at low levels (Fig. 3c). The vortex tilts downshear with height, with the center at 7.6 km altitude lying approximately 150 km southwest of the center at 0.6 km altitude.

b. Effect of varying vertical shear (S_L and S_U)

We first consider the effect of S_L and S_U, which control the vertical shear, temperature gradient, and moisture gradient in the lower and upper troposphere, respectively. Figure 4 shows the minimum pressure reached during the 6-day simulation for the dry (Fig. 4a) and moist (Fig. 4b) cases, as well as the 6-day accumulated rainfall (Fig. 4c). These metrics are shown as a function of S_L and S_U for $\zeta_0 = 1.0$, with the values of S_L and S_U having been selected by trial and error in order to capture a

wide range of behaviors. The range of S_U is wider than that of S_L, because our experiments are more sensitive to S_L than to S_U. Upon closer inspection, we found that simulations in the lower-right corner of Fig. 4b ($S_L < -1.0$ and $S_U < -2.0$) exhibited small-scale pressure minima coincident with the heaviest rainfall, but well displaced from the main circulation center. Since we consider these minima to be unrepresentative of the intensity of the larger-scale vortex, the pressure values shown in Fig. 4b are the minimum values within a $2° \times 2°$ box centered on the centroid of negative perturbation pressure at 1.5 km altitude.

The dry simulations reveal the extent to which the vortex amplifies in the absence of convection (Fig. 4a). We will show in section 3c(1) that this growth is primarily from barotropic instability. With an initial pressure anomaly of -1.3 hPa, this process contributes an additional -1.3 to -2.2 hPa to the anomaly. The dry vortex weakens as $|S_L|$ and $|S_U|$ increase, though only 0.9 hPa separates the strongest from the weakest experiment.

Including moisture leads to a stronger vortex for all simulations, with S_L and S_U substantially affecting the magnitude of this amplification (Fig. 4b; note the change in color scale compared to Fig. 4a). As $|S_L|$ increases, minimum pressure decreases, indicating a stronger vortex. Sensitivity to S_U is more complicated, with no obvious pattern emerging when comparing individual rows of constant S_L. However, considering the much larger range of S_U, vortex intensity is clearly more sensitive to S_L. Based on the monsoon low and depression track dataset of Vishnu et al. (2020), the 994 to 998 hPa surface pressures seen here are within the range of typical monsoon lows and depressions (Fig. 5). However, considering that a substantial number of observed monsoon depressions reach pressures below 994 hPa, the simulated ones are on the weaker side of normal. Additional analysis suggests that interactive surface fluxes of heat and moisture are required to reach these higher intensities (not shown). The pattern of accumulated rainfall is similar to that of minimum pressure, but with much larger differences across the parameter space (Fig. 4c). For example, total rainfall increases approximately tenfold as S_L goes from 0.0 to -1.5, whereas the magnitude of the pressure anomalies increases by less than a factor of 2.

To illustrate how S_L and S_U affect the vortex structure, Fig. 6 shows the 1.5 km total pressure and surface rain rate for each simulation at day three, a time near the peak vortex intensity. In cases with significant rainfall, the highest rain rates are located a few hundred kilometers southwest of the circulation center. By contrast, rainfall is substantially lighter and more randomly distributed about the circulation center for $S_L = 0$ when $|S_U| < 4.5$. These patterns are consistent with the fact that a vortex embedded in vertical shear generates its maximum ascent in its downshear-left quadrant (e.g., Rao and Rajamani 1970; Raymond 1992). The longitudinal distance between the rain and the circulation center increases with $|S_U|$, presumably as a result of differential advection caused by the strengthening vertical shear. The rain rate is highest in the lower-left corner of the plot, where $|S_U|$ is small and $|S_L|$ is large. However, as suggested by Fig. 4c, this pattern does not

(a) Min. Pressure (Dry)

(b) Min. Pressure (Moist)

(c) Total Rainfall (Moist)
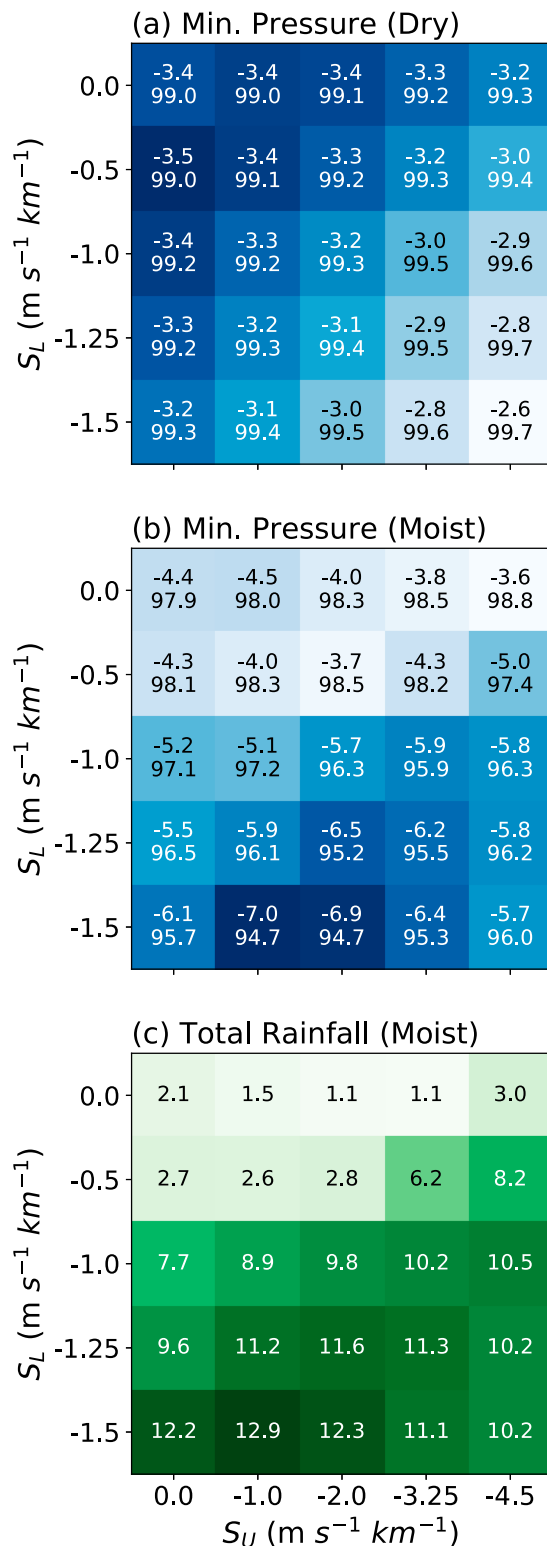
FIG. 4. Minimum pressure (hPa) and 6-day total rainfall (mm) as a function of vertical shear for $\zeta_0 = 1.0$. (a) Pressure for the dry experiments, (b) pressure for the moist experiments, and (c) rain for the moist experiments. Pressure is given as both the perturbation value at 1.5 km (upper number) and the total value at the
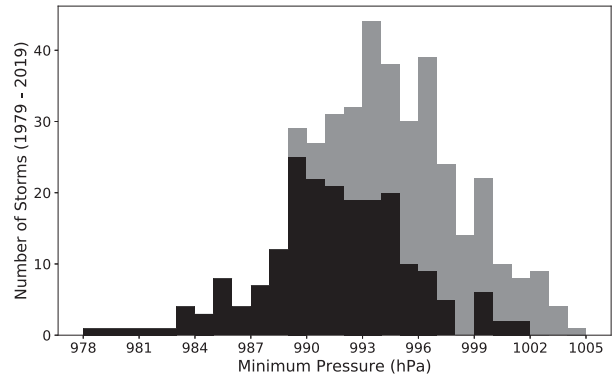
FIG. 5. Stacked histogram of number of monsoon lows and depressions in the Bay of Bengal from 1979 to 2019 binned by minimum pressure (hPa) reached during their life-span. Black bars show monsoon depressions and gray bars show monsoon lows. The black and gray bars are nonoverlapping. Dataset and classification based on Vishnu et al. (2020) and the hourly ERA5.

indicate that total accumulated rainfall decreases with $|S_U|$; the rain rate simply peaks before this instant in time for simulations with higher $|S_U|$.

To better understand the temporal coevolution between rainfall and vortex intensity as S_L and S_U vary, we examine time series of the previously shown metrics for select experiments. Specifically, we examine minimum perturbation pressure and rain rate for all values of S_L with S_U held constant at −2.0 (Figs. 7a,b) and for all values of S_U with S_L held constant at −1.0 (Figs. 7c,d). The parameter ζ_0 is held constant at 1.0 for all of these simulations. The thick lines show the moist simulations and the thin lines show the dry simulations.

We first discuss variations in S_L (Figs. 7a,b). Throughout the first day, the minimum pressure for each simulation is nearly identical (Fig. 7a) and little to no precipitation falls (Fig. 7b), indicating that only dry processes are contributing to growth. We show in section 3c(1) that this growth results from barotropic instability. The simulations begin to diverge on day 2. The moist ones become much stronger than the dry ones and variations in S_L lead to systematic differences within these two subgroups. For the dry experiments, increasing $|S_L|$ leads to slightly weaker vortices. For the moist experiments, increasing $|S_L|$ leads to substantially stronger vortices with higher rain rates. Temporally, this intensification is strongly linked to rain rates, with the rapid increase in rain on day 2 corresponding to falling pressure and the rapid decrease in rain on days 3 and 4 corresponding to rising pressure. Interestingly, there seems to be a bifurcation point between $S_L = −0.5$ and $S_L = −1.0$, with the two simulations with $S_L > −1.0$ behaving similarly and remaining less than 1 hPa deeper than their dry counterparts.

←

surface (lower number), expressed without the first digit (e.g., 993.8 hPa = 93.8). The total rainfall is averaged within a $10° \times 10°$ box centered on the minimum pressure. All values are the average of the two vortices.
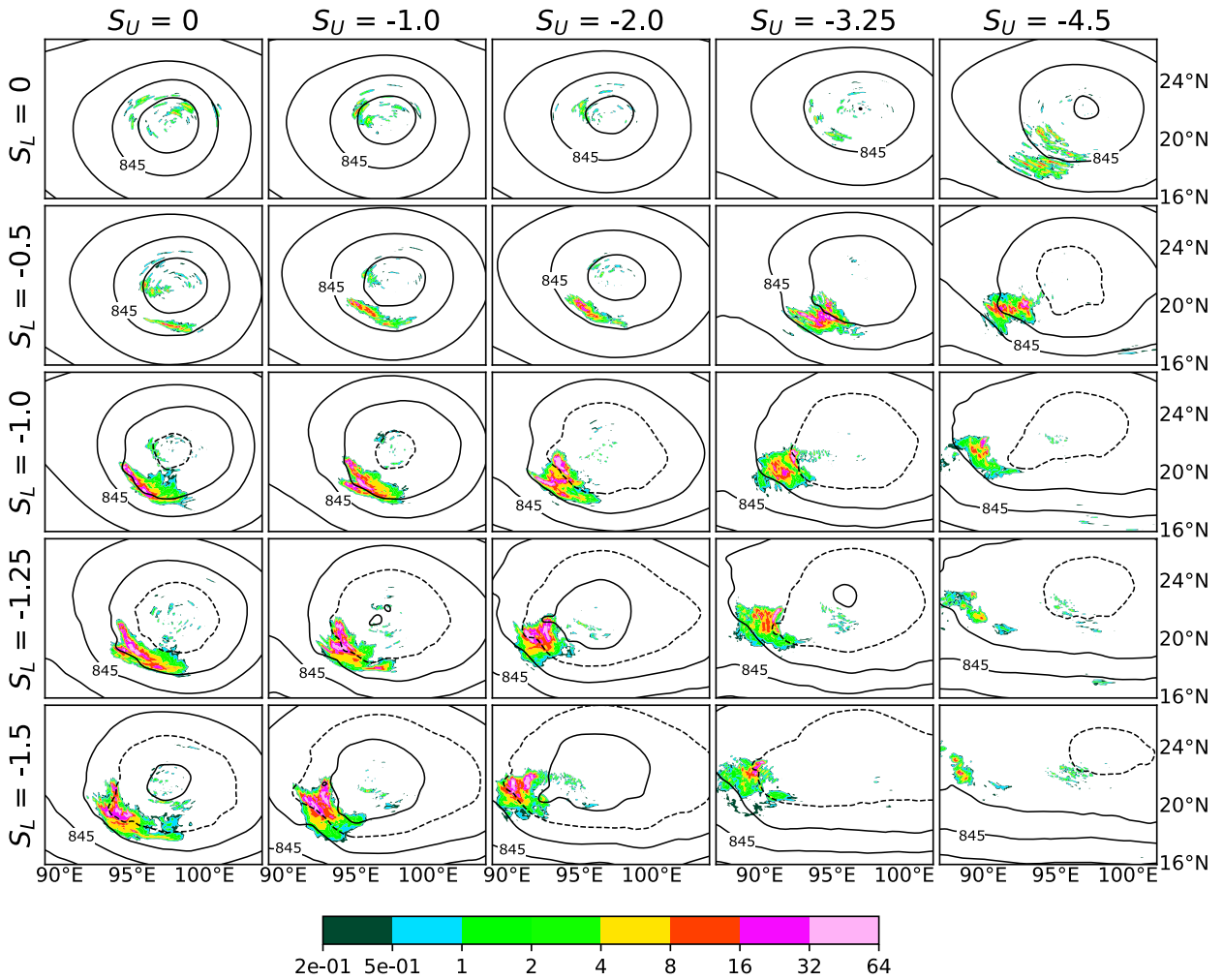
FIG. 6. Rain rate (shading, mm h^{-1}) and total pressure (contoured every 1.5 hPa) for all experiments with $\zeta_0 = 1.0$ at day 3 of simulation. The dashed contour corresponds to 842 hPa, marked to ease intercomparison of panels.

A possible explanation is that some threshold for convective initiation is crossed between these two values.

The simulations with varying S_U exhibit many of the same patterns as those with varying S_L (Figs. 7c,d). A notable difference is that the moist experiments with higher $|S_U|$ reach their peak intensity and highest rain rates earlier than those with lower $|S_U|$. In fact, those with lower $|S_U|$ eventually catch up in intensity to those with higher $|S_U|$, leading to the small differences in intensity seen in Fig. 4b. Examining Fig. 4, it appears that increases in upper-level shear (S_U) cause the precipitation to become increasingly detached from the circulation center, limiting the potential for the precipitation and the vortex to constructively interfere.

1) POTENTIAL ENERGY

Given the strong coupling between pressure and temperature through hydrostatic balance, determining the source of temperature anomalies can provide insight into what physical processes are responsible for the pressure anomalies in our

simulations. To do this, we derive an equation for potential energy in terms of θ' by multiplying Eq. (1b) by

$$A \equiv \frac{g}{\theta_0} \frac{\theta'}{d\theta_0/dz}. \tag{6}$$

The perturbation potential energy is then defined as

$$P'_e \equiv \frac{1}{2} \frac{g}{\theta_0} \frac{\theta'^2}{d\theta_0/dz} \tag{7}$$

with its time tendency given by

$$\frac{\partial P'_e}{\partial t} + (\overline{\mathbf{U}} + \mathbf{u}') \cdot \nabla P'_e = -Av' \frac{\partial \overline{\theta}}{\partial y} - gw' \frac{\theta'}{\theta_0} + AM'_\theta + AT'_\theta, \tag{8}$$

which has been simplified for a zonally symmetric basic state. The first two terms on the left-hand side (lhs) of Eq. (8) represent the local time tendency and advection of P'_e, respectively. The first term on the right-hand side (rhs) represents the conversion of basic-state potential to perturbation potential energy through
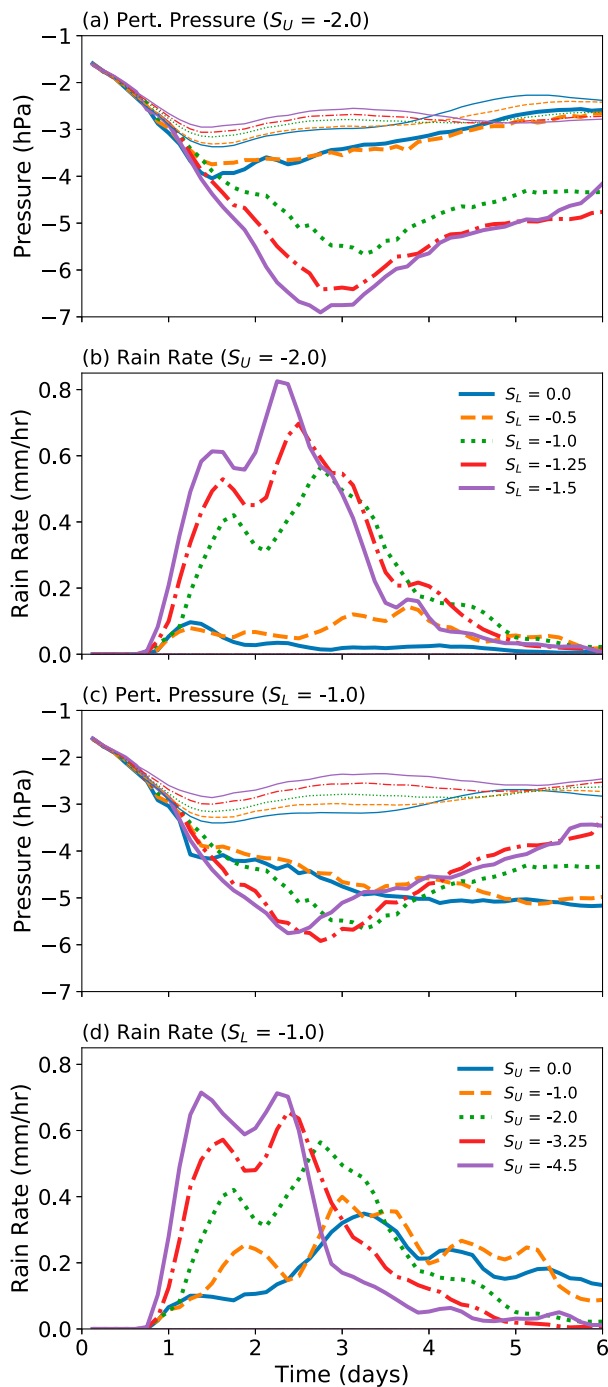
FIG. 7. Comparison of time series of minimum pressure and rain rates for select experiments. (a) Minimum pressure (hPa) for each value of S_L with $S_U = -2.0$ and $\zeta_0 = 1.0$ and (b) rain rates (mm h^{-1}) for the same experiments. Thick lines are for simulations with microphysics and thin lines for those without. (c),(d) As in (a) and (b), respectively, but for each value of S_U with $S_L = -1.0$. Rain rates are calculated using the same averaging box as in Fig. 4.
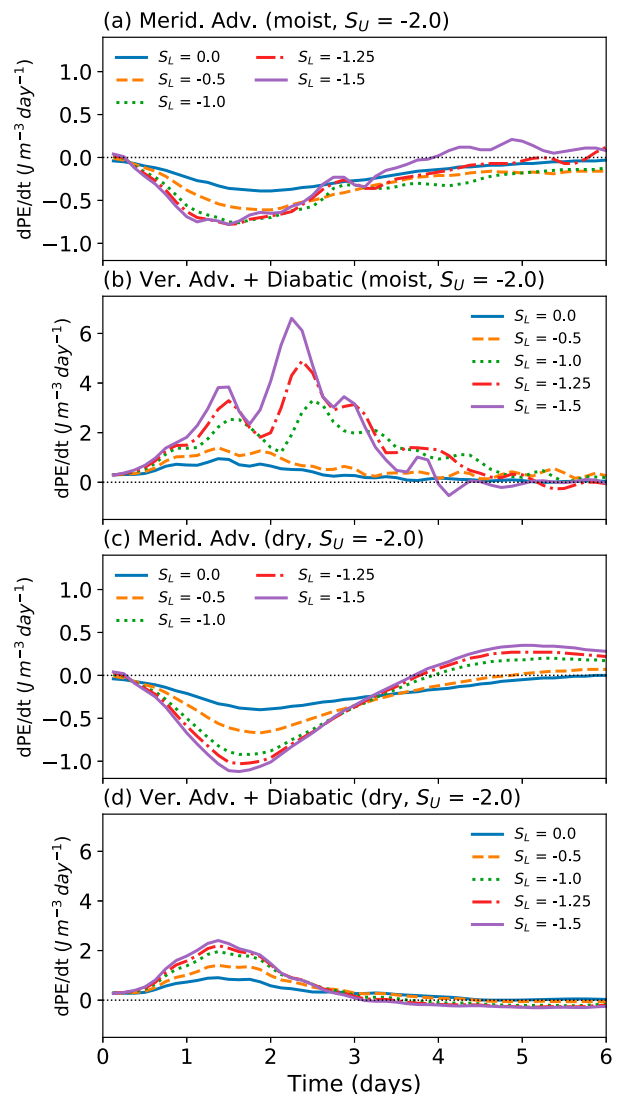
FIG. 8. Select terms in the potential energy equation integrated from the surface to 10.0 km and averaged over the full model domain. (a) Meridional advection [first term on rhs of Eq. (8)] and (b) vertical temperature advection plus diabatic terms [last three terms on rhs of Eq. (8)] for each value of S_L with S_U held constant at −2.0 and ζ_0 held constant at 1.0 for the moist simulations. (c),(d) As in (a) and (b), respectively, but for the dry simulations.

meridional advection of basic-state temperature. This process is fundamental to baroclinic instability. The second term represents the conversion of perturbation potential to perturbation kinetic energy through baroclinic conversion. Both baroclinic instability and diabatic heating from moist convection can contribute to this term. The third and fourth terms represent contributions to perturbation potential energy from microphysics and parameterized turbulent diffusion, respectively. This equation is useful for our purposes, because it can tell us the relative importance of baroclinic instability versus moist convection in generating the temperature anomalies by comparing the meridional advection term with the terms associated with diabatic heating. Figure 8 shows a

time series of select terms in Eq. (8) for each value of S_L with S_U held constant at -2.0. Each quantity is vertically integrated from the surface to 10.0 km and averaged over the full model domain. We combine the last three terms on the rhs of Eq. (8), because the diabatic and vertical advection terms strongly cancel (i.e., adiabatic cooling cancels condensational heating), and because turbulent diffusion is a substantial energy sink in regions of moist convection. For our case, this combination does not cause ambiguity, because almost all of the baroclinic conversion (term 2 on the rhs) is located within regions of moist convection as opposed to regions of meridional temperature advection, where term 1 on the rhs could be important.

Figure 8a demonstrates that this disturbance is not drawing energy from the meridional temperature gradient, indicating that it is not a baroclinic instability. In fact, consistent with the downshear tilt seen in Fig. 3, it is losing energy through $-A\upsilon'\partial_y\overline{\theta}$, with these losses generally growing with increasing $|S_L|$. Instead, the dominant energy source is diabatic heating from convection (Fig. 8b). This source becomes larger as $|S_L|$ increases and closely follows variations in the rain rates (Fig. 7b). However, not all of this energy comes from diabatic heating; the dry simulations also exhibit a peak in this term (Fig. 8d). This potential energy at least partly represents that required to bring the temperature field into thermal wind balance with the growing perturbation kinetic energy gained from the meridional shear [refer to section 3c(1)]. Some could also result from Ekman pumping or a vertical circulation induced by the vertical shear tilting the vortex. Interestingly, the $S_L = 0.0$ and $S_L = -0.5$ experiments are very similar between the dry and moist simulations, reinforcing the idea that moist convection has a minimal effect in amplifying these vortices.

2) RELATIONSHIP BETWEEN MOISTURE AND PRECIPITATION

Having established a strong relationship between S_L and rainfall, we now seek to understand what causes this trend. As a starting point, we examine the perturbation water vapor field in relation with the condensate field. Figure 9 shows vertically integrated condensate (Figs. 9a–d) and q_v' at 1.0 km above the surface (Figs. 9e–h) two days into the simulation for four different experiments in which only S_L varies. A clear trend emerges: anomalies of low-level moisture increase with $|S_L|$. In the bottom two rows of Fig. 9, the largest positive q_v' values are positioned just north of the largest condensate, with northerly flow advecting this moisture toward the convection. Such an arrangement is less apparent in the top two rows of Fig. 9, which display much weaker convection. Recall from section 3b that these two cases with $|S_L| < 1.0$ produce substantially less rainfall than those with higher $|S_L|$. On the eastern side of the circulation, where there is much less condensate, q_v' is mostly negative.

An intuitive way to understand the source of these q_v' anomalies is through a back trajectory analysis. To sample air parcels flowing into the convection, we initialize trajectories within a box bounded by 20°, 21°N, 91.5°, and 97.5°E (shown by red box in Fig. 9g) for vertical levels between 0.61 and 3.1 km for the simulation with $S_L = -1.0$. These parcels are followed backward from hour 48 to hour 0. The trajectories are then grouped according to their height at hour 48 and averaged to get a set of composite trajectories. Since we are most concerned with how parcels behave before reaching the convection, those that become saturated are excluded from this composite. Of the 2926 trajectories initially present at each vertical level, this subsetting leaves anywhere from nearly 100% of the trajectories below 1.3 km to 66%–69% above 1.8 km, with a rapid drop-off in between. Figure 10a shows a cross section of the trajectories colored by q_v', along with contours of basic-state potential temperature $(\overline{\theta} + \theta_0)$ and mixing ratio $(\overline{q_v} + q_0)$. The trajectories generally ascend while following a path closely parallel to the basic-state isentropes, though crossing at a slight angle below about 1.5 km. Since we have intentionally excluded most diabatic processes from this analysis, the ascent is almost entirely isentropic, with the deviations of the trajectories from the basic-state isentropes seen in Fig. 10a resulting from the isentropes themselves being advected southward. As trajectories follow isentropes, they cross contours of $\overline{q_v} + q_0$, raising their value of q_v'. This crossing explains the anomalies of q_v' seen in Fig. 9 and suggests an explanation of why q_v' varies strongly with increasing $|S_L|$: since the basic-state temperature and moisture gradients sharpen as $|S_L|$ increases, the angle between them steepens, enhancing the southward advection of moisture along an isentrope. This process is likely akin to that described in Adames and Ming (2018b).

As some theories of monsoon depression growth rely on horizontal moisture advection (e.g., Adames and Ming 2018a; Clark et al. 2020), it is useful to quantify how much this process contributes to the q_v' anomaly compared to that from vertical advection. We can calculate these quantities by deriving a Lagrangian version of our water vapor equation. The conservation equation for q_v' [Eq. (1d)] can be rewritten as

$$\frac{\partial q_v'}{\partial t} + (\overline{\mathbf{U}} + \mathbf{u}') \cdot \nabla q_v' = -\mathbf{u}' \cdot \nabla \overline{q_v} - w'\frac{dq_0}{dz} + M'_{q_v} + T'_{q_v}. \quad (9)$$

Simplifying for a zonally symmetric basic state yields

$$\frac{dq_v'}{dt} = -\upsilon'\frac{\partial \overline{q}}{\partial y} - w'\left(\frac{dq_0}{dz} + \frac{\partial \overline{q_v}}{\partial z}\right) + M'_{q_v} + T'_{q_v}, \quad (10)$$

which is an equation for q_v' following the flow. In this form, meridional and vertical advection of basic-state moisture become source terms for q_v' that can be integrated with time to determine their individual contributions. An analogous equation can be derived for θ'. Calculations for both q_v' and θ' are shown in Fig. 10b, which displays the average value for each trajectory composited in Fig. 10a integrated from hour 0 to hour 48. From Fig. 10b, it is clear that most of the q_v' comes from horizontal advection. For trajectories ending at 1 km, 69.5% of q_v' comes from horizontal advection and 29.2% from vertical advection with a residual of 1.1%. The difference between these two sources shrinks with height, with both contributing nearly equally by 3 km. Consistent with isentropic ascent, the source terms of θ' largely cancel, though with increasing warm advection below 2 km (cf. Fig. 3c, which shows a
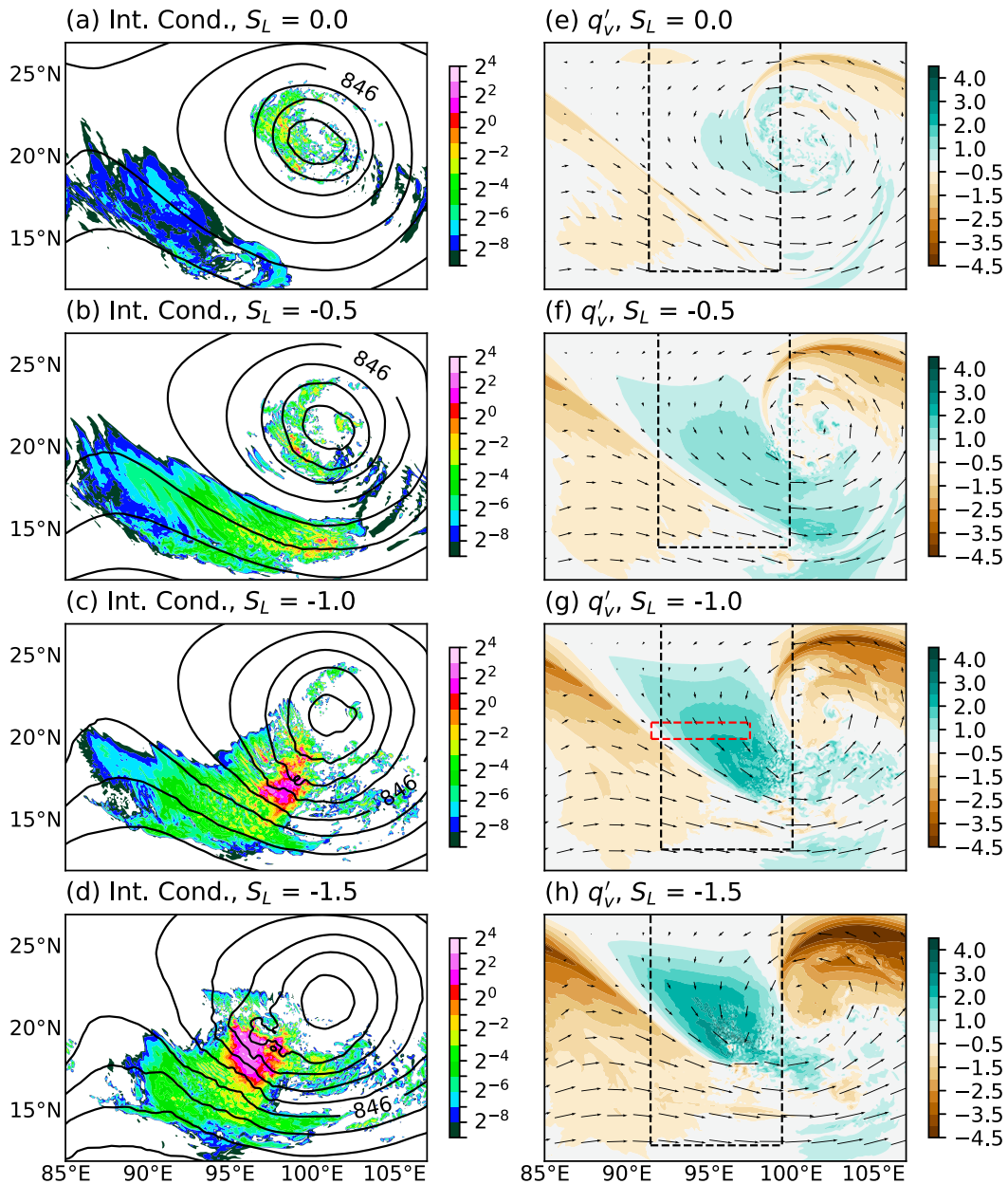
FIG. 9. Comparison among simulations for $S_U = -2.0$ and $\zeta_0 = 1.0$ as S_L varies. (a)–(d) Vertically integrated condensate (shading, $q_c + q_r + q_s + q_i$, g kg^{-1}) from the surface to 15.0 km and total pressure (contoured by 1.0 hPa, at 1.5 km) for values of $S_L = 0$, -0.5, -1.0, and -1.5 at hour 48. (e)–(h) Perturbation mixing ratio (shading, q'_v, g kg^{-1}) and winds (vectors) at 1.0 km for the same set of simulations. The black boxes show the bounds used to calculate the MSE budgets for this time in section 3b(3), with the northernmost edge extending past the figure bounds. The red box shows the starting point of the back trajectories in section 3b(2).

warm anomaly west of the low-level cold core) and increasing cold advection above 2 km.

3) MOIST STATIC ENERGY BUDGETS

Though the trajectory analysis is intuitive and visually appealing, using it to compare multiple simulations evolving with time is cumbersome. To better quantify the relationships between convection and moisture, we use a vertically integrated

MSE budget. Such an analysis is beneficial because several recent studies have applied it to idealized simulations of monsoon depressions (e.g., Adames and Ming 2018b; Clark et al. 2020). We define a basic-state MSE by

$$\overline{h} \equiv c_p(\overline{\tau} + \tau_0) + L_v(\overline{q_v} + q_0) + gz \qquad (11)$$

and a perturbation MSE by
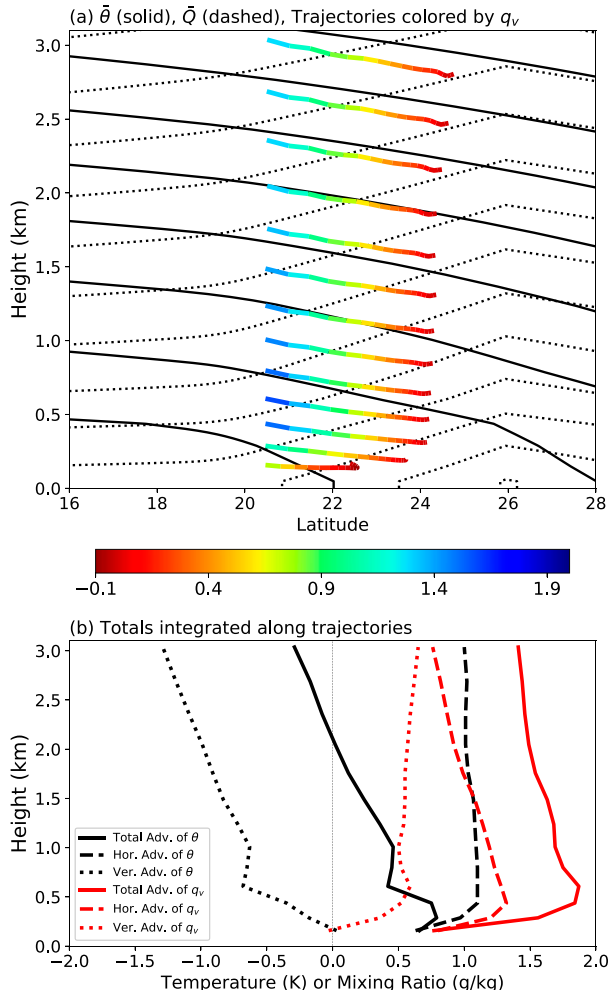
FIG. 10. Trajectory analysis. (a) Composite trajectories colored by perturbation mixing ratio (q_v', g kg^{-1}) with basic-state potential temperature (contoured by 2.0 K, $\bar{\theta} + \theta_0$) in solid contours and basic-state mixing ratio (contoured by 1.0 g kg^{-1}, $\overline{q_v} + q_0$) in dashed contours. (b) Accumulated contributions of vertical and horizontal advection to the perturbation potential temperature (θ', K) and perturbation mixing ratio (q_v', g kg^{-1}) as a function of the trajectories' height at hour 48. A box showing the starting point of the trajectories is drawn in Fig. 9g.

$$h' \equiv c_p \tau' + L_v q_v', \qquad (12)$$

where $c_p = 1004.0$ J kg^{-1} K^{-1}, $L_v = 2.5 \times 10^6$ J kg^{-1}, and τ is temperature. The full budget of h' simplified for a zonally symmetric basic state is

$$\frac{\partial h'}{\partial t} = -\overline{\mathbf{V}} \cdot \nabla_2 h' - \mathbf{v}' \cdot \nabla_2 h' - v'\frac{\partial \overline{h}}{\partial y}$$

$$+ \left[-w'\frac{\partial(\overline{h} + h')}{\partial z} + M_h' \right] + T_h', \qquad (13)$$

where ∇_2 is the two-dimensional gradient operator, $\overline{\mathbf{V}}$ is the two-dimensional wind, and the square brackets enclose two terms that we will combine. As the vortex interacts with the $\overline{h}$

gradient, it creates both positive and negative MSE anomalies. Since the positive anomalies are more important for understanding how the convection evolves, we isolate them by drawing a box from the centroid of negative pressure at 1.5 km to 8° west of this point, and from 8° to the north of the centroid's latitude to 8° to its south. Figure 9 shows this box in relation to the 1.5 km q_v' anomalies, which are collocated with h' anomalies (not shown). We average over this box and calculate a mass-weighted average from the surface to 18.2 km. It will also be useful to divide MSE into its dry static energy (DSE; $c_p \tau'$) and moisture ($L_v q_v'$) components. This analysis is shown in Fig. 11 for the simulation with $S_L = -1.0$ and $S_U = -2.0$, chosen because it lies in the middle of the parameter space. As with our previous budgets, the values represent three hour accumulated tendencies converted to daily rates.

Over the course of the simulation, h' increases for about 1.5 days and then decreases, becoming negative after day 3 (Fig. 11a). Its magnitude and sign are dominated throughout by $L_v q_v'$ (Fig. 11b), though $c_p \tau'$ makes some contribution after day 2 (Fig. 11c). Comparing with the rain time series (Fig. 7b, green dotted line), we see that the initial rapid increase in rain rate occurs just after h' peaks, then h' decreases during the period of intense rain and becomes negative just before the rain rate decreases. This correspondence suggests a causal relationship between the buildup of h' and the ensuing convection. The initial buildup is driven primarily by horizontal advection of basic-state MSE ($v'\partial_y \overline{h}$) (Figs. 11a,d), which increases both $c_p \tau'$ and $L_v q_v'$ (Figs. 11e,f). The subsequent decrease in h' is also produced by horizontal advection: once significant q_v' anomalies develop, nonlinear horizontal advection and advection of q_v' by the basic state both become large and negative (Fig. 11e), overwhelming the $v'\partial_y \overline{h}$ term. This process can be inferred from Fig. 9g: westerlies advect drier air into the western side of the box and moister air out of the eastern side. Additionally, easterlies advect drier air through the eastern side of the box. Essentially, the initially straight contours of mixing ratio are deformed by the vortex to the point that horizontal advection no longer increases the vertically integrated moisture within the averaging box. Such a process does not occur with DSE, even though the temperature and moisture gradients are initially parallel, and horizontal DSE advection remains positive throughout the simulation (Fig. 11f). The explanation is clear from Fig. 10a; since the flow tends to follow isentropes, the temperature field is not nearly as strongly deformed as the moisture field.

The strong cancellation between vertical and horizontal advection of $c_p \tau'$ during the first few days (Figs. 11c,f) is consistent with the isentropic ascent discussed in section 3b(2). This ascent increases q_v' through vertical advection (Fig. 11b) and closely follows arguments by Adames and Ming (2018b). Compared with the isentropic analysis in section 3b(2), the vertically integrated moisture budget (Fig. 11b) yields a higher contribution from vertical advection than from horizontal advection. This discrepancy results at least partly from vertical moisture advection becoming larger above the region analyzed in section 3b(2). Additionally, the averaging box includes the convection, whose cross-isentropic flow would enhance vertical advection. The trajectory analysis sought to exclude this
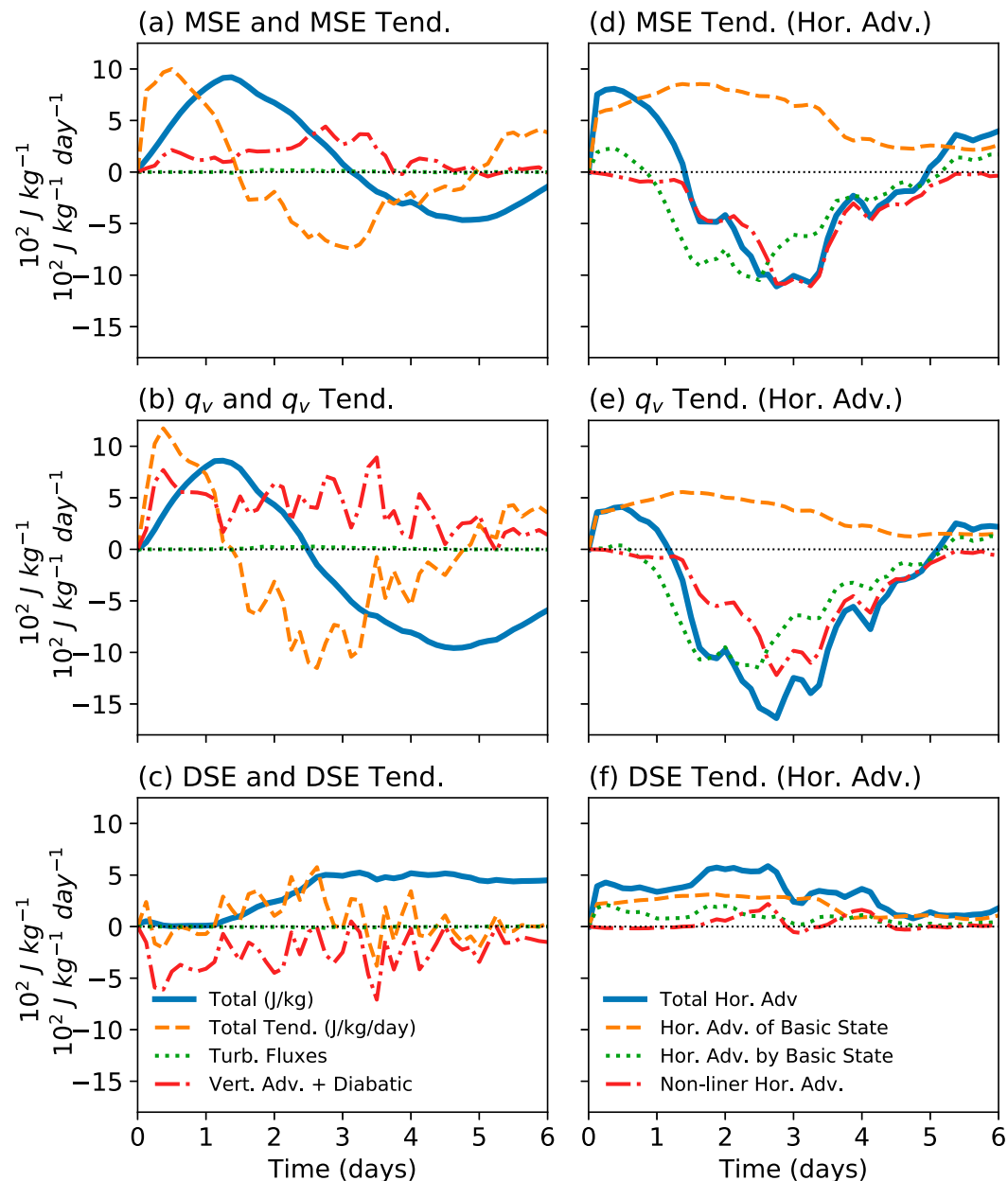
FIG. 11. Vertically integrated MSE budget (h') for $\zeta_0 = 1.0$, $S_L = -1.0$, and $S_U = -2.0$. (a) Total h' (J kg^{-1}), total h' tendency (J kg^{-1} day^{-1}), total vertical advection plus diabatic tendencies from microphysics [term 4 on rhs of Eq. (13)], and the subgrid-scale turbulent flux of h' [term 5 on rhs of Eq. (13)]. (b) As in (a), but for the $L_v q_v'$ component of h'. (c) As in (a), but for the $c_p \tau'$ component. (d) The total horizontal advection of h', the advection of the basic-state h [term 3 on rhs of Eq. (13)], the advection by the basic state of h' [term 1 on rhs of Eq. (13)], and the nonlinear advection of h' [term 2 on rhs of Eq. (13)]. (e),(f) As in (d), but for the $L_v q_v'$ and $c_p \tau'$ components, respectively. A box showing the horizontal extent of the averaging region at day 2 is drawn in Fig. 9g.

process. Interestingly, in contrast with the MSE analysis of Adames and Ming (2018b), we find that vertical advection increases h' in the precipitating region (Fig. 11a).

The close association between h' and convection may be used to explain the rainfall and vortex intensity differences among our simulations. Figure 12 shows vertically integrated h' and its horizontal advection for the same simulations shown in

Fig. 7, but with $S_L = -1.25$ omitted for clarity. A clear relationship exists between S_L and the buildup of h' during the first two days (Fig. 12a). This trend is best explained by the tendency for horizontal MSE advection to increase with $|S_L|$ (Fig. 12c), a pattern brought about by $|S_L|$ steepening the low-level $\bar{h}$ gradient. The strong relationship between MSE advection and precipitation likely explains why increasing $|S_L|$
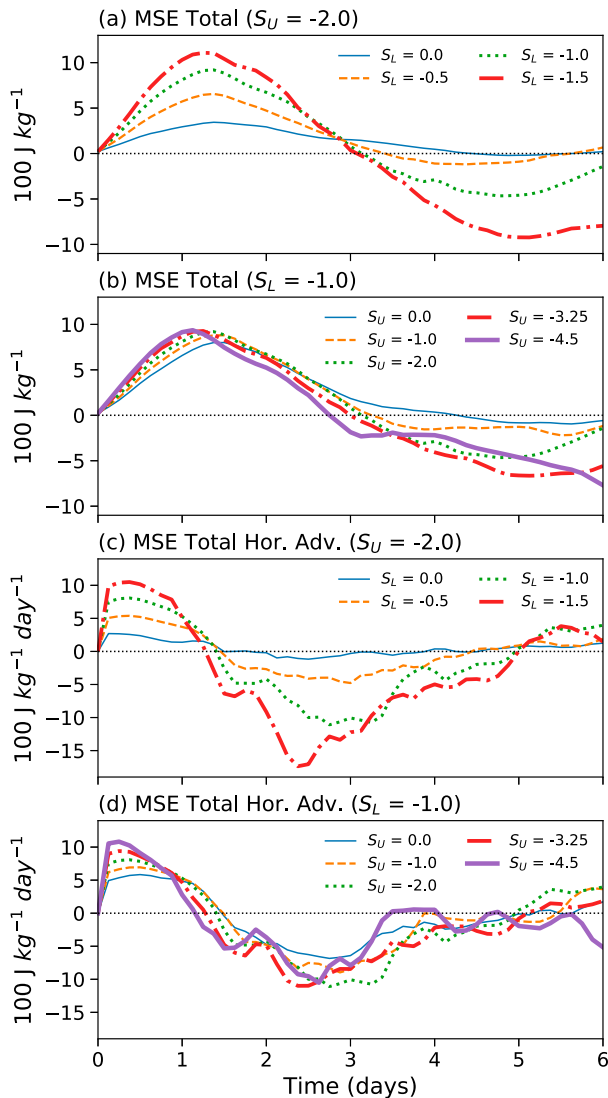
FIG. 12. Comparison of select terms in the vertically integrated MSE budget (h') for $\zeta_0 = 1.0$. (a) Total h' (J kg^{-1}) for $S_U = -2.0$ as S_L varies and (b) the same for $S_L = -1.0$ as S_U varies. (c) The total horizontal advection of h' (J g kg^{-1} day^{-1}) for the same experiments as (a), and (d) the total horizontal advection of h' for the same experiments as (b). A box showing the horizontal extent of the averaging region at day 2 is drawn in Fig. 9g.

enhances rainfall and vortex intensity. Such a pattern is less prominent for changes in S_U (Figs. 12b,d), perhaps because most processes important to convection in these simulations occur within the lower troposphere. The vortex and its associated temperature and moisture advection are strongest in the lower troposphere, where positively buoyant air parcels that trigger and maintain convection are located. These factors may partly explain why rainfall is much more sensitive to changes in S_L than in S_U (Fig. 4).

To further establish the relationship between rainfall and MSE advection, we compare the accumulated rainfall in all simulations to horizontal MSE advection, including for
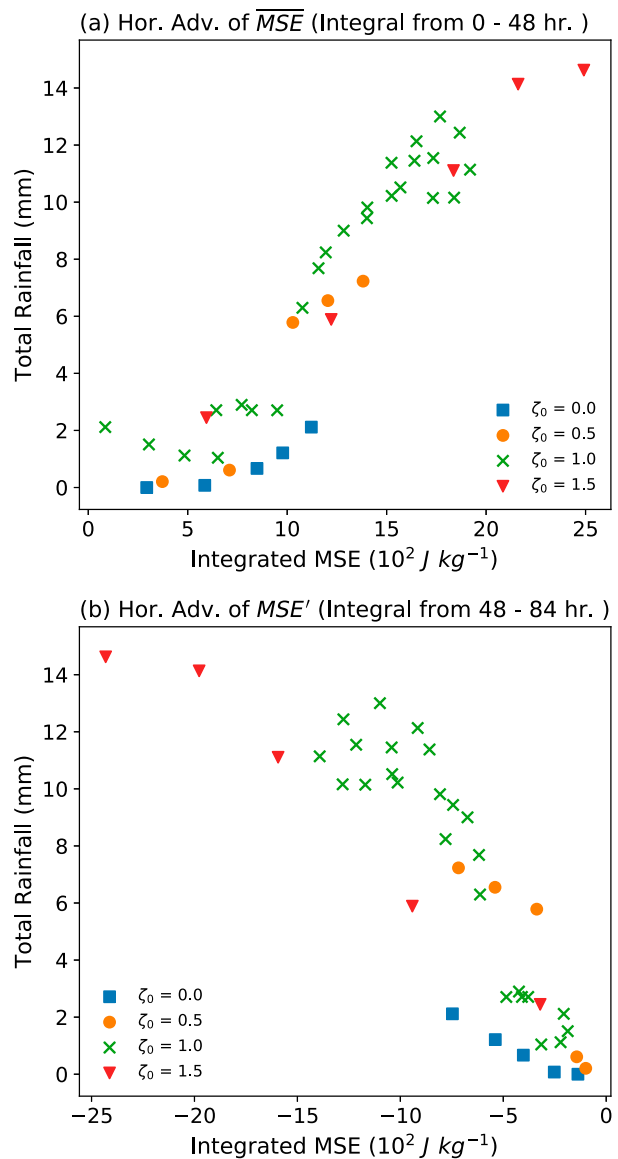
FIG. 13. Total accumulated rainfall (mm) for each 6-day simulation vs time-integrated horizontal MSE (h') advection (J kg^{-1} day^{-1}). (a) Advection of basic-state MSE [term 3 on rhs of Eq. (13)] integrated from 0 to 48 h and (b) advection of perturbation MSE by the basic-state and perturbation wind [terms 1 and 2 on rhs of Eq. (13)] integrated from 48 to 84 h. Rainfall calculated as in Fig. 4.

experiments in which we vary ζ_0 that are presented more thoroughly in section 3c. Figure 13a shows $-v'\partial_y\overline{h}$ integrated from hour 0 to 48 and Fig. 13b shows $-(\overline{\mathbf{V}} + \mathbf{v}') \cdot \nabla_2 h'$ integrated from hour 48 to 96. The MSE advection terms are calculated as discussed in section 3b(3) and the rainfall as done in Fig. 4. Rainfall increases as $-v'\partial_y\overline{h}$ goes up, a trend that persists for different values of ζ_0 (Fig. 13a). Interestingly, there is a gap between two clusters of simulations: one in the lower-left corner below 4 mm of rainfall and another in the upper-right above this value. This gap

suggests a threshold of h' must be reached before significant rainfall occurs, possibly related to the amount of ascent required to bring air parcels to their level of free convection. This gap is likely another manifestation of the bifurcation behavior noted in Fig. 7. The opposite trend occurs for the other two advection terms: they become increasingly negative with increasing rainfall (Fig. 13b). As suggested by Figs. 9 and 12c, the larger MSE gradients also lead to more dry air advection, ultimately limiting the growth of MSE anomalies and the time period over which the vortices can grow through convective coupling.

4) MOISTURE GRADIENT

In section 3b(2) we attributed a significant fraction of the vortex-generated MSE anomaly to horizontal moisture advection (Fig. 10b). This is intriguing in light of the results of Adames and Ming (2018a,b), which disagree on whether the more important moisture source is horizontal or vertical advection. We can test the importance of horizontal moisture advection in our simulations by altering the meridional moisture gradient. For our next experiments, we set the moisture gradient north of 15°N to zero. This cutoff latitude is a compromise between preventing the southern portion of the domain from becoming saturated and allowing most of the vortex, which is centered at 20°N, to lie within the zero-gradient region. We continue to impose the vertical moisture profile from the reanalysis at 20°N, so that flattening the moisture gradient in this manner reduces the mixing ratio and relative humidity north of 20°N and increases these quantities from 15° to 20°N. Other features of the basic state, including the wind and temperature remain unchanged. Results are shown in Fig. 14 for three simulations with different values of S_L with $S_U = -2.0$. For comparison, we also show a dry simulation and a moist simulation with an unaltered moisture gradient.

Flattening the moisture gradient reduces the peak vortex intensity by roughly a factor of 2, with the minimum pressure for $S_L = -1.0$ only slightly more intense than in the dry experiment (Fig. 14a). The $S_L = -1.5$ and $S_L = -1.25$ experiments yield similar pressure time series, indicating that much of the sensitivity of the simulations to S_L comes from changes in the moisture field. Flattening the moisture gradient also substantially reduces the rain rate (Fig. 14b). This reduction makes sense for at least two reasons: lowering the relative humidity of air parcels flowing from the north requires that they be lifted farther before becoming saturated, and the column integrated moisture of this inflow is also lower. However, rain rates still increase with $|S_L|$, suggesting that the basic-state temperature gradient and vertical shear enhance rainfall.

Designing an analogous experiment wherein the temperature gradient is flattened is more difficult, because the vertical shear and temperature gradient are linked dynamically. Also, reducing the temperature gradient without changing the moisture field would destabilize the atmosphere to moist convection to the north, where the temperature would have to be cooled substantially. So we refrain from altering the temperature gradient and conclude that the three experiments shown in Fig. 14 reveal that the vortex evolution is
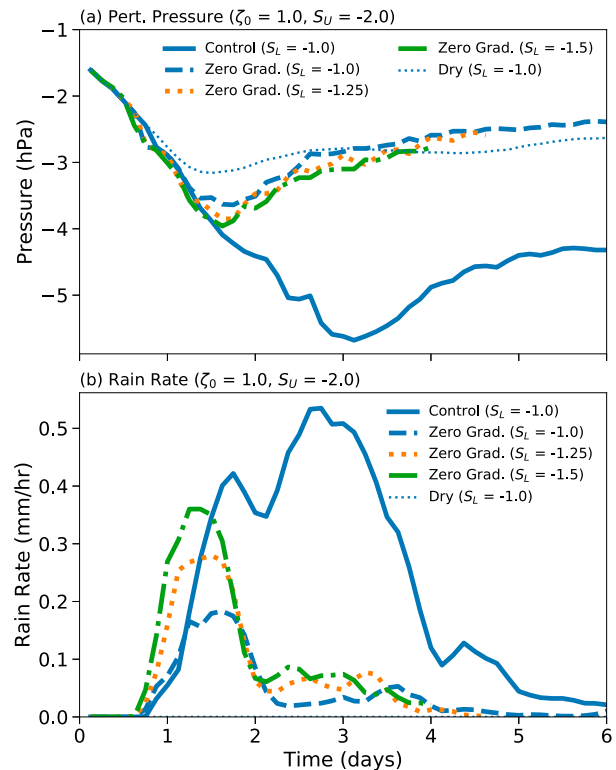
FIG. 14. For experiments with zero moisture gradient, time series of (a) minimum perturbation pressure (hPa) and (b) hourly rain rate (mm h^{-1}), calculated using the same averaging box as in Fig. 4. One experiment with an unaltered moisture gradient is plotted for comparison.

very sensitive to the moisture gradient. Despite this sensitivity, it is worth noting that one-third to one-half of the vortex's intensity seems to come from dry processes unrelated to the moisture gradient. In fact, for the first 24 h, almost none of the amplification requires moist convection. This growth phase is the focus of the next section.

c. Effect of varying meridional shear (ζ_0)

Our analysis has thus far focused on the impact of changing S_L and S_U for a fixed value of ζ_0, the parameter controlling low-level meridional shear. We now experiment with changing ζ_0. Since we found that vortex amplification is more sensitive to S_L than to S_U, we pair variations in ζ_0 with S_L. Figure 15 shows minimum pressure and total rainfall for this set of experiments, calculated in the same manner as in Fig. 4.

For the dry simulations, vortex intensity increases strongly with ζ_0 and generally decreases weakly with $|S_L|$ (Fig. 15a). We will show in section 3c(1) that this sensitivity exists, because the growth of the dry vortex results from barotropic instability. For moist simulations, the vortex becomes stronger and rainier for increases in both ζ_0 and $|S_L|$ (Figs. 15b,c). Comparing these two sets of experiments, the moist vortex is almost always stronger than the dry vortex, with the biggest differences in minimum pressure occurring when $|S_L|$ is large. As discussed in section 3b(3), this additional intensification is

(a) Min. Pressure (Dry)

(b) Min. Pressure (Moist)

(c) Total Rainfall (Moist)
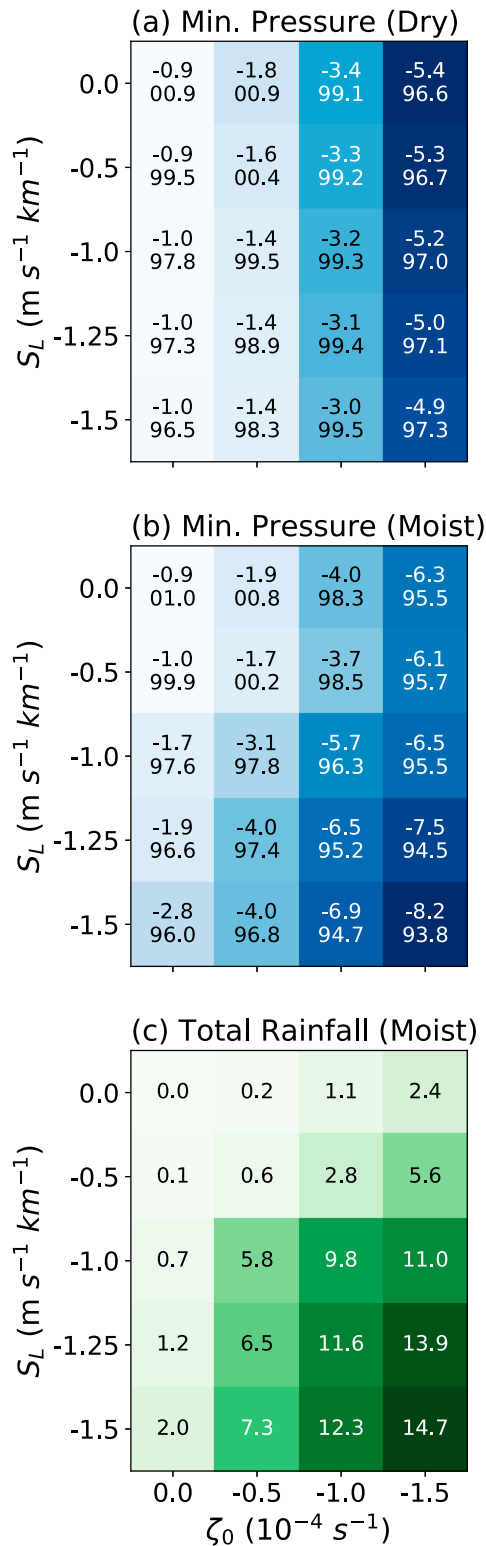
FIG. 15. As in Fig. 4, but for variations in ζ_0 vs variations in S_L.

caused by latent heat release from convection forced by MSE advection, a process that becomes more prominent with increasing $|S_L|$. The enhanced rainfall with increasing ζ_0 may also result from strengthening MSE advection. According to Fig. 15a, higher ζ_0 leads to a stronger vortex even without moisture, and the associated stronger wind would lead to more MSE advection, even if the MSE gradient remains fixed. As implied in section 2b(1), the low-level MSE gradient does not remain exactly fixed as ζ_0 is altered, but these changes are much smaller than that produced by altering S_L. For example, decreasing S_L from -1.0 to -1.5 increases the MSE gradient by approximately $2.35\,\mathrm{J\,kg^{-1}\,km^{-1}}$ at 20°N and 1.2 km altitude, whereas a change in ζ_0 from 0 to 1.5 alters it by only $0.52\,\mathrm{J\,kg^{-1}\,km^{-1}}$

The $\zeta_0 = 0$ simulations are especially instructive, because they represent the limiting case of a basic state featuring an MSE gradient without meridional shear. Since the initial disturbance begins with a $5\,\mathrm{m\,s^{-1}}$ wind anomaly, it still has the opportunity to generate convection through MSE advection, possibly leading to amplification. However, for $|S_L| < 1.0$, there is essentially no vortex growth relative to the dry experiments and almost no rainfall. For higher values of $|S_L|$, some amplification occurs relative to the dry case, indicating that the MSE advection process can act independently. Nevertheless, this growth is weak and does not lead to intensities meriting monsoon depression classification.

To determine how ζ_0 impacts vortex structure, we plot total pressure at 1.5 km altitude and rain rate at day 2.75 for each simulation (Fig. 16). As suggested by Fig. 15, the circulation becomes much more prominent as ζ_0 increases, with the pressure field evolving from an open trough at $\zeta_0 = 0$ to a vortex with a growing number of closed isobars as ζ_0 increases. In fact, disturbances for $\zeta_0 < 1.0$ hardly resemble monsoon depressions. Though much of the evolution in structure as ζ_0 increases is a consequence of the higher intensity of the perturbation flow, some of it results from sharpening of the basic-state trough of low pressure. Similar to the experiments in Fig. 6, the rainfall tends to be located in the southwest quadrant for cases with $|S_L| > 0$ and is largest for higher values of $|S_L|$. As with Fig. 6, we caution that the experiments exhibit maximum rain rates at different times. For example, peak rainfall for $\zeta_0 = 0$ occurs before the time shown.

To characterize how ζ_0 influences the temporal evolution of the vortex, we examine time series of minimum pressure and rain rate at constant $S_L = -1.0$ and $S_U = -2.0$ as ζ_0 varies. During the first day, the moist (thick lines) and dry (thin lines) experiments are nearly identical for a given ζ_0 (Fig. 17a). The amplification rate increases strongly with ζ_0, indicating that dry processes dominate growth within this early phase. Afterward, however, pressure curves for moist and dry experiments quickly diverge, with the dry experiments beginning to weaken or hold steady while the moist ones strengthen. This suggests that growth after the first 24–36 h is driven by coupling with moist convection, an assumption supported by the higher rain rates that accompany this continued strengthening (Fig. 17b). An exception is the $\zeta_0 = 0$ case, which only deviates from the
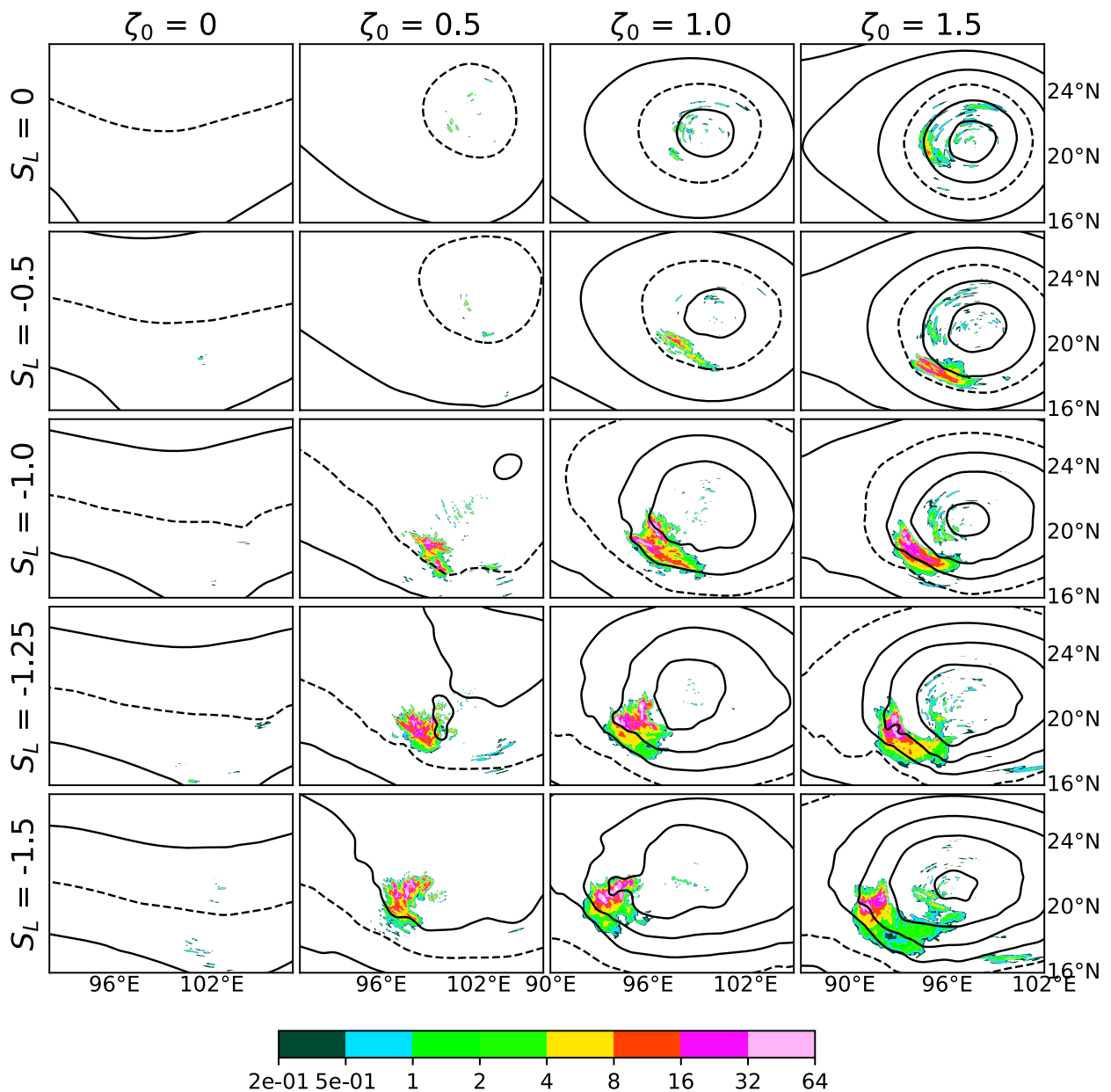
FIG. 16. As in Fig. 6, but for all experiments with $S_U = -2.0$ at day 2.75 of simulation. The dashed contour corresponds to 845 hPa and the contour interval is 1.5 hPa.

dry experiment during a short period when it produces rain. As the simulations continue, the strengthening ceases and rain rates approach zero toward day 6.

ENERGETICS

To explain why changes in ζ_0 affect the vortices, we examine the perturbation kinetic energy equation. The full version of this equation is described in detail in Diaz and Boos (2019b). In simulations presented here, the two primary source terms are $u'v' d_y \overline{U}$ and $\mathbf{v}' \cdot \nabla \phi'$, with all others being small or negative. The former is energy acquired from the basic-state meridional

shear and is linked to barotropic instability. The latter is energy from pressure work, linked to latent heat release by moist convection. Time series of both terms are shown in Fig. 18 for variations of ζ_0 at $S_L = -1.0$, and for $\zeta_0 = 1.0$ at $S_L = 0.0$ and -1.5.

As expected, the contribution of $u'v' d_y \overline{U}$ to the perturbation kinetic energy increases with ζ_0, the parameter that governs the strength of the low-level meridional shear (Fig. 18a). This suggests the presence of barotropic instability or barotropic growth. For nonzero ζ_0, this term is largest on day one, then falls to near or below zero by day 3.
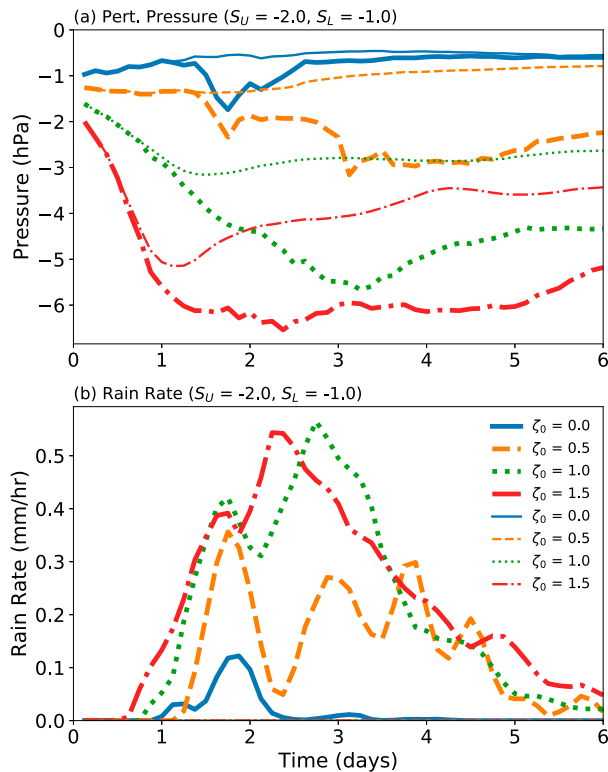
FIG. 17. Comparison of time series of minimum pressure and rain rates for select experiments. (a) Minimum pressure (hPa) for each value of ζ_0 with $S_U = -2.0$ and $S_L = -1.0$. Thick lines are for simulations with microphysics and thin lines for those without. (b) Rain rates (mm h^{-1}) for the same experiments as in (a), calculated using the same averaging box as in Fig. 4.

FIG. 18. Time series of select terms in the perturbation kinetic energy equation averaged over the full horizontal extent of the model domain below an altitude of 15 km. (a) The meridional shear term ($u'v'd_y\overline{U}$) for each value of ζ_0 with $S_U = -2.0$ and $S_L = -1.0$. Experiments for $\zeta_0 = 1.0$ and $S_U = -2.0$, but with $S_L = -1.5$ and 0.0 are also shown. (b) As in (a), but for the pressure work term ($\mathbf{v}' \cdot \nabla\phi'$).

This decrease presumably results from the growing disturbance stabilizing the basic-state meridional shear. During the second half of the simulation, only the highest shear case ($\zeta_0 = 1.5$) continues growing from this term. By contrast, $\mathbf{v}' \cdot \nabla\phi'$ starts near zero to slightly negative and then becomes positive after day 1 (Fig. 18b), roughly following rain rates (Fig. 17). Its magnitude grows with increasing $|S_L|$ and ζ_0, consistent with these trends resulting in more rainfall (cf. Fig. 15c).

Interestingly, the contribution from $u'v'd_y\overline{U}$ to the perturbation kinetic energy seems to be governed almost exclusively by ζ_0; the time series for $\zeta_0 = 1$ are nearly identical as S_L varies from 0.0 to −1.0 to −1.5 (Fig. 18a). This similarity suggests that growth of the vortex through barotropic processes unfolds independently of convection. In other words, additional strengthening of the vortex from latent heat release does not feed back on barotropic growth. This lack of a feedback seems reasonable, because the period during which latent heat release contributes most strongly to growth does not coincide with the period when barotropic growth is most active (Fig. 18). By contrast, increasing ζ_0 has a strong impact on $\mathbf{v}' \cdot \nabla\phi'$, presumably because stronger perturbation winds produced by more barotropically unstable basic states lead to greater MSE advection, thus generating more convection.

4. Summary and discussion

Our experiments reveal that, for sufficiently strong low-level MSE gradients and meridional shears, a regime exists where a disturbance can grow by drawing energy from both the basic-state meridional shear and the disturbance's interaction with moist convection. From our analysis, we can describe its basic life cycle. Growth over the first day comes almost entirely from barotropic instability as the initial modal structure draws energy from the basic-state meridional shear. In the presence of a meridional MSE gradient, the growing perturbation advects temperature and moisture. On the western side of the vortex, perturbation northerlies advect moisture southward and upward along sloping isentropes, leading to saturation and convection southwest of the vortex center. Latent heat release amplifies the vortex in ways not discussed in detail here, but which may be consistent with the diabatic heating being biased into the warm part of the westward-propagating wave by a convective time lag (Adames and Ming 2018a) or with the diabatically generated potential vorticity being nonlinearly advected toward the vortex center (Diaz and Boos 2019b; Dunkerton et al. 2009). This process results in a peak intensity three days into the simulation. By this time, initially straight moisture contours have become so distorted that meridional advection dries the convecting region, causing the rain rate to fall and the vortex to spin down.

Consistent with this life cycle, two parameters exert strong control over the intensity of the vortex and its rainfall. The first is the strength of meridional shear, which controls the barotropic stability of the basic state. The second is the magnitude of the low-level MSE gradient, which controls the extent to which latent heat release amplifies the vortex. To the degree that these idealized experiments represent South Asian monsoon depressions, they suggest that juxtaposition of a strong MSE gradient with the enhanced meridional shear of the monsoon trough makes the South Asian monsoon especially favorable to depression growth.

The process in our simulations by which convection is forced by moisture advection along sloping isentropes is essentially that discussed in Adames and Ming (2018b). However, there are differences. Whereas they found that vertical advection is the source of moistening within the vortex, our simulations have contributions from both vertical and horizontal advection, with the latter dominating. In fact, when horizontal moisture advection is eliminated by removing the moisture gradient, little intensification occurs even though isentropic ascent can still act. This outcome is more consistent with the analytical theory of Adames and Ming (2018a), which is an extension of Sobel et al.'s (2001) concept of "moisture modes." Nevertheless, these differences might not be contradictory. The analysis of Adames and Ming (2018b) included only the time when the vortex was near peak intensity. If one examined only the time of peak intensity in our simulations, one would also find horizontal temperature advection causing vertical moisture advection, with horizontal moisture advection being negative. Such a state is more in line with their results. Differences could also be attributed to the fact that our trajectory analysis examines a subsaturated region whereas Adames and Ming (2018b) examines a region of moist convection, where vertical moisture advection is likely stronger. Additionally, the normal-mode theory used in Adames and Ming (2018b) is valid only for small-amplitude disturbances, a condition that better characterizes the earliest development phase. Consistently, meridional moisture advection is an MSE source for only the first day of our simulation, after which the vortex has deformed the moisture gradient to the point that nonlinear terms dominate. In contrast with these two studies, however, our results suggest that MSE advection alone does not lead to substantial growth; removing meridional shear entirely resulted in anemic growth with disturbances that do not resemble monsoon depressions. Even for cases with the strongest growth, the MSE advection process is self-limiting and amplifies the vortex only up to the lower range of intensities of observed monsoon depressions.

Our results bear some similarity to those of Diaz and Boos (2019b) in that disturbances grow from the combined effects of barotropic instability and moist convective coupling. However, there are some crucial differences. First, we do not find states that are barotropically stable without convection but unstable with convection; all states that we presented with nonzero meridional shear are barotropically unstable, if only marginally so. One potential explanation for this discrepancy is that the period of growth through barotropic instability and that through convective coupling are separated in time and therefore these processes cannot reinforce one another. A second possible explanation lies in our use of zonal symmetry. A more realistic basic state with a zonally confined region of strong meridional shear surrounded by weaker shear would have different stability characteristics than one that is zonally uniform (Diaz and Boos 2019a). Another discrepancy with Diaz and Boos (2019b) is their emphasis on QG ascent alone as the mechanism that maintains convection. While QG ascent exists in our simulations, the fact that removing the moisture gradient limits the convection and halts vortex growth suggests that a poleward moisture gradient is important. In other words, lifting of moisture by QG ascent is insufficient.

As with any idealized modeling study, there are caveats. As mentioned above, the South Asian monsoon is not zonally uniform. Specifically, the ends of the monsoon trough exhibit enhanced curvature vorticity that often rolls up into vortices, and this structure seems related to the mean monsoon circulation. With a zonally uniform state, such rollup is more difficult to achieve by anything other than barotropic instability. Thus, our experiments could overemphasize the importance of barotropic instability, although stable barotropic rollup might still be necessary for growth. Additionally, there is some artificiality in starting with a subsaturated atmosphere. Enhanced meridional shear in the monsoon trough is often accompanied by enhanced convection. Thus, the temporal separation between growth from shear and growth from convection in our experiments could be an artifact of the experimental setup. Furthermore, this study does not consider the role of surface sensible and latent heat fluxes. Despite these caveats, our experiments suggest that monsoon depression amplification requires both barotropic growth due to meridional shear and moist convective coupling that arises through advection of a meridional MSE gradient.

Data availability statement. The numerical model simulations upon which this study is based are too large to archive or to transfer. However, the model source code, along with instructions on how to compile and run it, are provided at https://github.com/michaeldiaz0/Model.

REFERENCES

Adames, Á. F., and Y. Ming, 2018a: Interactions between water vapor and potential vorticity in synoptic-scale monsoonal disturbances: Moisture vortex instability. *J. Atmos. Sci.*, **75**, 2083–2106, https://doi.org/10.1175/JAS-D-17-0310.1.

——, and ——, 2018b: Moisture and moist static energy budgets of South Asian monsoon low pressure systems in GFDL AM4.0.

J. Atmos. Sci., **75**, 2107–2123, https://doi.org/10.1175/JAS-D-17-0309.1.

Clark, S. K., Y. Ming, and Á. F. Adames, 2020: Monsoon low pressure system–like variability in an idealized moist model. *J. Climate*, **33**, 2051–2074, https://doi.org/10.1175/JCLI-D-19-0289.1.

Diaz, M., and W. R. Boos, 2019a: Barotropic growth of monsoon depressions. *Quart. J. Roy. Meteor. Soc.*, **145**, 824–844, https://doi.org/10.1002/qj.3467.

——, and ——, 2019b: Monsoon depression amplification by moist barotropic instability in a vertically sheared environment. *Quart. J. Roy. Meteor. Soc.*, **145**, 2666–2684, https://doi.org/10.1002/qj.3585.

Ditchek, S. D., W. R. Boos, S. J. Camargo, and M. K. Tippett, 2016: A genesis index for monsoon disturbances. *J. Climate*, **29**, 5189–5203, https://doi.org/10.1175/JCLI-D-15-0704.1.

Dunkerton, T., M. Montgomery, and Z. Wang, 2009: Tropical cyclogenesis in a tropical wave critical layer: Easterly waves. *Atmos. Chem. Phys.*, **9**, 5587–5646, https://doi.org/10.5194/acp-9-5587-2009.

Fujinami, H., H. Hirata, M. Kato, and K. Tsuboki, 2020: Mesoscale precipitation systems and their role in the rapid development of a monsoon depression over the Bay of Bengal. *Quart. J. Roy. Meteor. Soc.*, **146**, 267–283, https://doi.org/10.1002/qj.3672.

Hong, S.-Y., J. Dudhia, and S.-H. Chen, 2004: A revised approach to ice microphysical processes for the bulk parameterization of clouds and precipitation. *Mon. Wea. Rev.*, **132**, 103–120, https://doi.org/10.1175/1520-0493(2004)132<0103:ARATIM>2.0.CO;2.

Kessler, E., 1969: *On the Distribution and Continuity of Water Substance in Atmospheric Circulations*. Springer, 84 pp.

Monteiro, J. M., and J. Sukhatme, 2016: Quasi-geostrophic dynamics in the presence of moisture gradients. *Quart. J. Roy. Meteor. Soc.*, **142**, 187–195, https://doi.org/10.1002/qj.2644.

Mooley, D., and J. Shukla, 1989: Main features of the westward-moving low pressure systems which form over the Indian region during the summer monsoon season and their relation to the monsoon rainfall. *Mausam*, **40**, 137–152.

Moorthi, S., and A. Arakawa, 1985: Baroclinic instability with cumulus heating. *J. Atmos. Sci.*, **42**, 2007–2031, https://doi.org/10.1175/1520-0469(1985)042<2007:BIWCH>2.0.CO;2.

Nitta, T., and K. Masuda, 1981: Observational study of a monsoon depression developed over the Bay of Bengal during summer MONEX. *J. Meteor. Soc. Japan*, **59**, 672–682, https://doi.org/10.2151/jmsj1965.59.5_672.

Rao, K., and S. Rajamani, 1970: Diagnostic study of a monsoon depression by geostrophic baroclinic model. *Indian J. Meteor. Geophys.*, **21**, 187–194.

Raymond, D., 1992: Nonlinear balance and potential-vorticity thinking at large Rossby number. *Quart. J. Roy. Meteor. Soc.*, **118**, 987–1015, https://doi.org/10.1002/qj.49711850708.

Rutledge, S. A., and P. Hobbs, 1983: The mesoscale and microscale structure and organization of clouds and precipitation in midlatitude cyclones. VIII: A model for the "seeder-feeder" process in warm-frontal rainbands. *J. Atmos. Sci.*, **40**, 1185–1206, https://doi.org/10.1175/1520-0469(1983)040<1185:TMAMSA>2.0.CO;2.

Saha, K., and C. Chang, 1983: The baroclinic processes of monsoon depressions. *Mon. Wea. Rev.*, **111**, 1506–1514, https://doi.org/10.1175/1520-0493(1983)111<1506:TBPOMD>2.0.CO;2.

Sobel, A. H., J. Nilsson, and L. M. Polvani, 2001: The weak temperature gradient approximation and balanced tropical moisture waves. *J. Atmos. Sci.*, **58**, 3650–3665, https://doi.org/10.1175/1520-0469(2001)058<3650:TWTGAA>2.0.CO;2.

Vishnu, S., W. Boos, P. Ullrich, and T. O'Brien, 2020: Assessing historical variability of South Asian monsoon lows and depressions with an optimized tracking algorithm. *J. Geophys. Res. Atmos.*, **125**, e2020JD032977, https://doi.org/10.1029/2020JD032977.